ADVANCED MATERIALS
www.advmat.de

Advancing Catalysts by Stacking Fault Defects for Enhanced Hydrogen Production: A Review

Yuan Wang, Tian Wang, Hamidreza Arandiyan,* Guoqiang Song, Hongyu Sun, Ylias Sabri, Chuan Zhao, Zongping Shao, and Sibudjing Kawi**

Green hydrogen, derived from water splitting powered by renewable energy such as solar and wind energy, provides a zero-emission solution crucial for revolutionizing hydrogen production and decarbonizing industries. Catalysts, particularly those utilizing defect engineering involving the strategical introduction of atomic-level imperfections, play a vital role in reducing energy requirements and enabling a more sustainable transition toward a hydrogen-based economy. Stacking fault (SF) defects play an important role in enhancing the electrocatalytic processes by reshaping surface reactivity, increasing active sites, improving reactants/product diffusion, and regulating electronic structure due to their dense generation ability and profound impact on catalyst properties. This review explores SF in metal-based materials, covering synthetic methods for the intentional introduction of SF and their applications in hydrogen production, including oxygen evolution reaction, photo- and electrocatalytic hydrogen evolution reaction, overall water splitting, and various other electrocatalytic processes such as oxygen reduction reaction, nitrate reduction reaction, and carbon dioxide reduction reaction. Finally, this review addresses the challenges associated with SF-based catalysts, emphasizing the importance of a detailed understanding of the properties of SF-based catalysts to optimize their electrocatalytic performance. It provides a comprehensive overview of their various applications in electrocatalytic processes, providing valuable insights for advancing sustainable energy technologies.

1. Introduction

1.1. Generation Mechanism of Hydrogen

Hydrogen is the cleanest and most promising energy carrier to replace traditional fossil fuels.[1] Compared to coal, gasoline, or other clean energies (e.g., CH_4, C_2H_5OH), hydrogen has the highest energy density due to its negligible molecular weight. Furthermore, the only by-product after hydrogen combustion is water, achieving zero emission of CO_2. Hydrogen fuel cell technology has made significant advancements[2] with the recent introduction of hydrogen-fueled vehicles by Toyota and Hyundai[3] demonstrating the growing importance of hydrogen energy. Compared with other hydrogen generation technologies, water electrolysis shows many unique advantages.[4] Solar energy or electricity from renewable energy approaches can greatly facilitate hydrogen production, allowing high-purity hydrogen to be produced on a large scale without emitting CO_2. Conversely, water is the only raw material produced in the process, eliminating the limitations of the technology related

---

Y. Wang
Department of Chemical Engineering
The University of Melbourne
Parkville, VIC 3010, Australia
E-mail: helena.wang@unimelb.edu.au

Y. Wang, T. Wang, G. Song, S. Kawi
Department of Chemical & Biomolecular Engineering
National University of Singapore
Singapore 117585, Singapore
E-mail: chekawis@nus.edu.sg

The ORCID identification number(s) for the author(s) of this article can be found under https://doi.org/10.1002/adma.202313378

DOI: 10.1002/adma.202313378

H. Arandiyan
Centre for Advanced Materials and Industrial Chemistry (CAMIC)
School of Science
RMIT University
Melbourne, VIC 3000, Australia
E-mail: hamid.arandiyan@rmit.edu.au

H. Arandiyan
Laboratory of Advanced Catalysis for Sustainability
School of Chemistry
University of Sydney
Sydney, NSW 2006, Australia

H. Sun
DENSsolutions B.V.
Informaticalaan 12, 2628 ZD, Delft Netherlands

Y. Sabri
Centre for Advanced Materials and Industrial Chemistry (CAMIC)
School of Engineering
RMIT University
Melbourne, VIC 3000, Australia

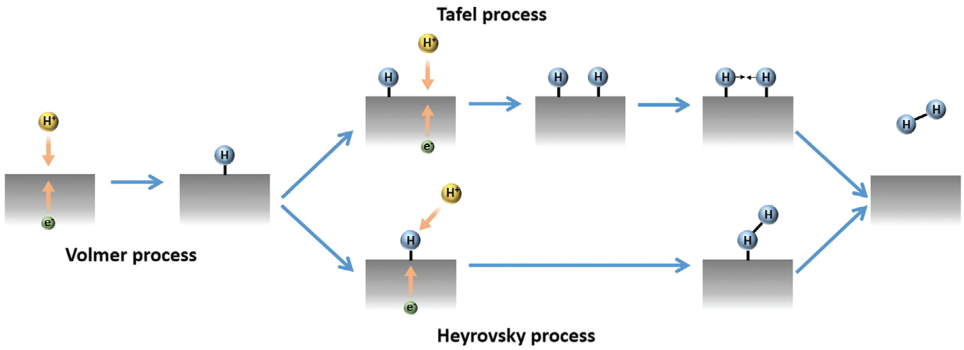

Figure 1. Scheme of mechanisms of HER.

to location, raw material prices, and other factors. Finally, to ensure the electron and charge balance of the water electrolysis reaction, high-purity oxygen, which is also an important chemical feedstock, will be generated in the other (anodic) chamber. Generally, in acid electrolytes, the reaction kinetics of the hydrogen evolution reaction (HER) are much faster (2,3 order) than in alkaline electrolytes due to the presence of a large number of H_3O^+ ions with weak covalent bonds. However, HER under acidic conditions has the following disadvantages: i) expansion of the acid-resistant proton-exchange membrane (PEM); ii) high risk in strong acid operation conditions; iii) potential corrosion issues under acid conditions; iv) volatile acids causing potential contamination issues. Therefore, despite the sluggish reaction kinetics, HER under alkaline conditions has been widely studied, and great progress has been made.[5]

The HER is a multi-step process on the electrode surface. As shown in **Figure 1**, the first step is called the Volmer process, where a proton source couples with an electron on a free active site on the electrode to generate an adsorbed hydrogen (*H). H_2 molecules can then be formed through two different approaches. The first approach is called the Heyrovsky mechanism (Bottom of Figure 1). Specifically, the formed *H will proceed to another proton-coupled electron transfer step (PCET) to generate a hydrogen molecule, desorbed from the electrode surface. The second approach is named the Tafel mechanism (Top of Figure 1). Under this circumstance, the Volmer process requires the formation of another adsorbed hydrogen atom *H near the first *H. Two adjacent *H sites will then combine to form a hydrogen molecule and desorb from the electrode surface. The rate-determine step (RDS) of HER can be easily evaluated by calculating the Tafel slope from the Butler–Volmer equation. If the RDS is a Tafel process (two adjacent *H combined), the Tafel slope should be 2.3RT/2F, giving a value of 29 mV dec^{-1} at room temperature (25 °C). If the RDS is a Heyrovsky process (*H goes through another PCET step), the Tafel slope should be 4.6RT/3F, giving a value of 38 mV dec^{-1} at 25 °C. If the RDS is a Volmer process (first PCET to form *H), then the Tafel slope should be 4.6RT/F, giving a value of 116 mV dec^{-1} at 25 °C.

As another half-reaction of water electrolysis, oxygen evolution reaction (OER) has also received widespread attention because it can be coupled with many reduction reactions, including HER, carbon dioxide reduction reaction (CO_2RR), nitrate reduction reaction (NO_3RR), and nitrogen reduction (NRR). Similarly, OER can also occur in acidic and alkaline electrolytes. In acidic electrolytes, H_2O molecules act as an oxygen source and produce H^+ as a by-product. In comparison, the OH^- anion can offer oxygen by producing H_2O as a by-product. The major advantages of acidic PEM electrolyzers are compact cell structure, low resistance, large current, and good gas purity.[6] Meanwhile, alkaline electrolyzers also have the advantages of low cost, high OER activity, and robust stability.[7] For convenience, this section only introduces the reaction mechanism in acidic electrolytes. For metal or alloy catalysts, two possible reaction pathways for OER are displayed in **Figure 2a**. In the first step, H_2O molecules are adsorbed on the active site M of the catalyst to form M—OH species. At the same time, H^+ and electrons will be released and enter the electrolyte and circuit, respectively. The formed M—OH will further undergo an electron-coupled H^+ removal process. Therefore, M—O species can be formed. The M—O can then combine with another adjacent M—O species (top of Figure 2) and release O_2 molecules into the electrolyte, similar to the Tafel process in HER. Alternatively, M—O species can also undergo a similar electron-coupled H^+ removal process with the assistance of H_2O to form M—OOH. Finally, O_2 molecules can be generated by an additional electron-coupled H^+ removal process (bottom of Figure 2). This mechanism is called the adsorbate evolution mechanism (AEM). Recently, in light of the remarkable OER performance exhibited by many metal oxide catalysts, another reaction mechanism for OER on metal oxides has been proposed.[8] As shown in Figure 2b, the lattice oxygen evolution mechanism is elucidated. Unlike a single active site in the AEM, lattice oxygen in metal oxides also participates in the OER. Therefore, the active site is expressed as O—M—O instead of M. A similar electron-coupled H^+ removal process is performed by adding H_2O to O—M—OOH. After the next electron-coupled H^+ removal step, O—M—OO species can be generated. Subsequently, O_2 molecules can be released directly to the electrolyte by leaving oxygen vacancies on the catalyst surface. After two similar electron-coupled

---

C. Zhao
School of Chemistry
The University of New South Wales
Sydney, NSW 2052, Australia

Z. Shao
WA School of Mines: Minerals
Energy and Chemical Engineering
Curtin University
Perth, WA 6845, Australia

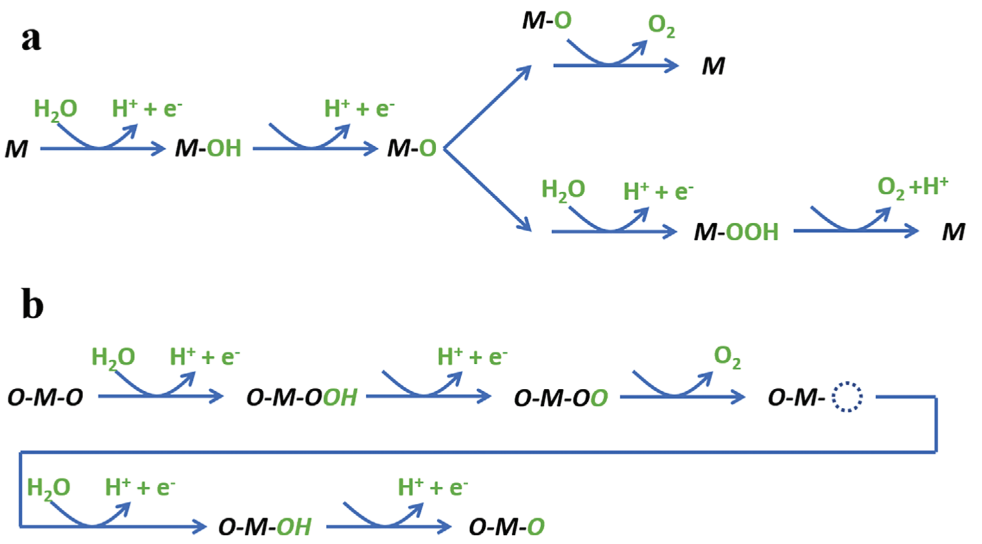

Figure 2. Scheme of mechanisms of OER a) adsorbate evolution mechanism, and b) lattice oxygen evolution mechanism.

H^+ removal steps, the oxygen vacancies can be filled to restore the catalyst structure. Since lattice oxygen also participates in the reaction, the original adsorption energy scaling relationship between M—OH and M—OOH can be broken, and the catalytic OER performance may be significantly improved.

1.2. Roles and Classification of Defects in Catalysis

During heterogeneous catalytic reactions, chemical transformations occur at the heterogeneous interfaces between electrocatalytic materials and reactants, spanning solid/liquid, solid/gas, and solid/liquid/gas interfaces. Within these interfaces, the conversion of reactants involves steps such as diffusion, adsorption, chemical reaction, and desorption. The physical and chemical properties of catalysts significantly affect these processes. Designing optimal material structures and understanding catalyst-reaction relationships are critical for heterogeneous catalytic research. Over time, catalyst enhancement strategies, including crystal facet manipulation,[9] interface engineering,[10] strain engineering,[11] and defect engineering[12] control have been explored. Defect engineering has emerged as a particularly significant and effective avenue to enhance catalytic activity by precisely tuning the electronic and geometric configurations of materials.[13] The defective sites play a dual role, not only serving as active sites for adsorbing intermediate reactive species but also as “docking” sites that attract and stabilize heteroatoms, leading to the formation of synergetic coordination structures and thus the creation of new active sites.[14]

By dimension, defects can be divided into the following categories: 0D point defects, such as oxygen vacancies and cation site vacancies; 1D linear defects, like dislocations; 2D planar defects, including stacking faults (SFs), grain/phase boundaries, and twin boundaries; and 3D volumetric defects, such as micropores/mesopores/macropore, surface voids.[15] 3D volumetric defects are more macroscopic, and there is little difference in the microscopic reaction environment interface of the catalytic reaction between the 3D defect surface and the non-defect surface. Among the various types of defects, 2D planar defects have the most significant influence on altering the intrinsic catalytic reaction, as they can be generated volumetrically and typically have high defect density, which distinguishes them from 0D and 1D counterparts. SF defects, in particular, not only appear at high density, thus providing more active sites (regions with exposed edge or step sites) but also trigger adjustments in electronic structure modification (such as electron density distribution and band structure),[16] induce strain (thus influencing the binding energy of adsorbed species),[17] promote surface reactivity (via formation of coordination sites),[18] and even enhance mass transport (functioning as diffusion pathways for reactants and products).[19] Since SF can lead to complex interactions of structural, electronic, and chemical effects, thereby significantly enhancing electrocatalytic performance, they have been widely explored for different electrochemical reactions, such as HER,[19] OER,[20] overall water splitting,[21] oxygen reduction reaction (ORR),[22] NO_3RR,[23] and energy storages.[24]

SFs are interruptions in the regular arrangement of crystal planes, often stacked on top of each other, causing crystallographic anomalies.[25] The crystal structure can be conceptualized as a consistent sequence stack of planes following a repetitive motif, constituting what is known as a stacking sequence.[26] For example, in a face-centered cubic (FCC) lattice, the stacking arrangement of (111) planes follows the sequence of ABCABCABC, as depicted in **Figure** 3a,b. Deviations from this prescribed sequence result in SF (see Figure 3c,d). These faults behave either as intrinsic faults, involving the removal of a plane and resulting in the sequence of ABCACABC, or as extrinsic faults, requiring the insertion of an additional plane, resulting in the sequence ABCACBABC. When the SF does not span the whole crystal, it is constrained by one or two dislocations. These partial dislocations have a unique Burgers vector called a Shockley dislocation (refer to Figure 3e,f), which is characterized by a/6[112] type rather than a direct translation of the lattice. Under certain circumstances, the regular ABCABCABC sequence may locally transform into a symmetrical structure like CBACBACBA, which usually occurs during processes such as solidification

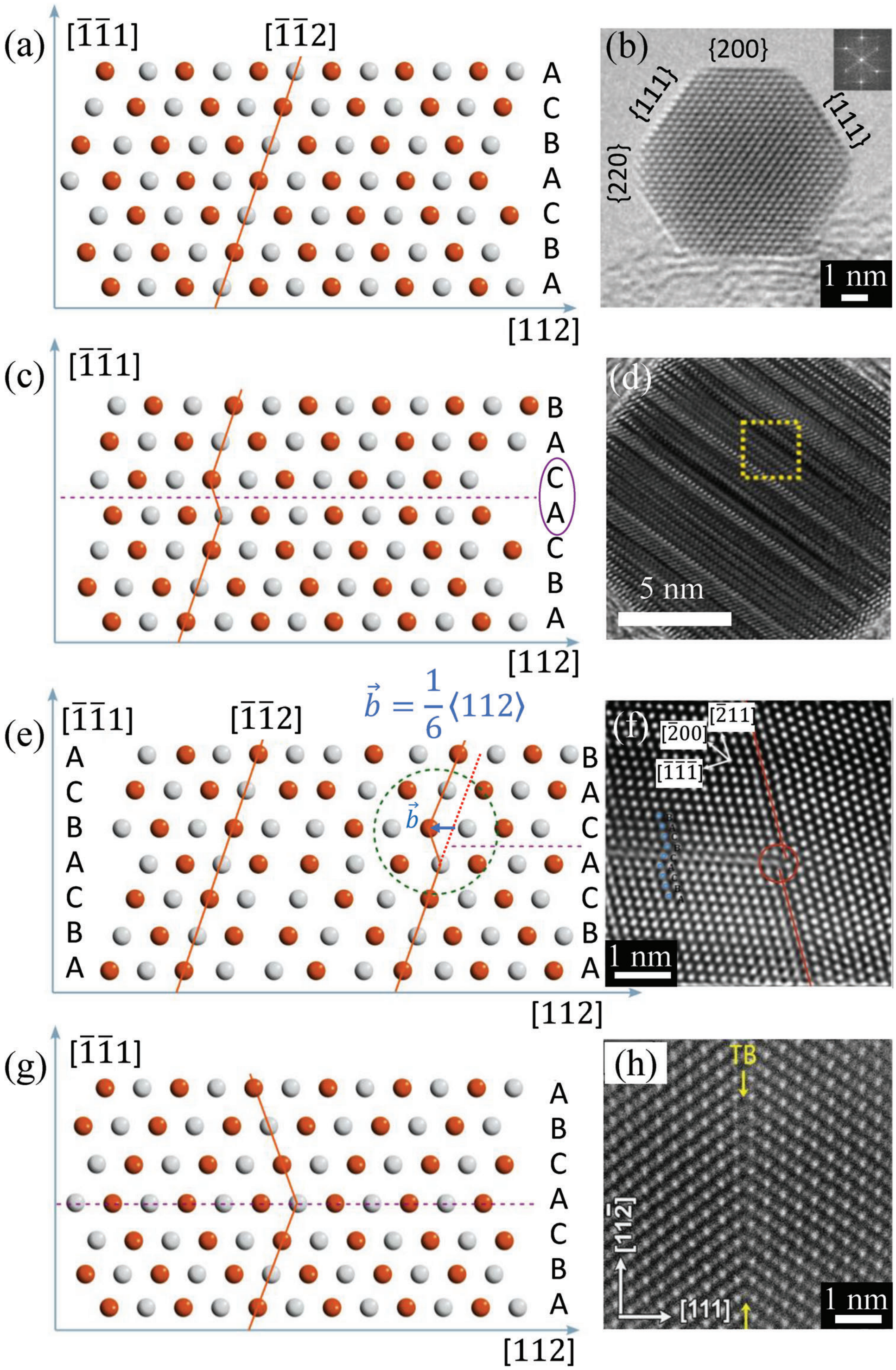

Figure 3. a) Scheme of a stack of closely packed (111) planes in the FCC lattice.[26] b) High-resolution transmission electron microscopy (HRTEM) image of an AgI nanoparticle captured along the <110> zone axis, inset showing the FFT of the nanoparticle. Reproduced with permission.[27] Copyright 2013, Elsevier. c) Scheme of superlattice intrinsic SF in an FCC structure.[26] d) TEM image of SF-Ru. Reproduced with permission.[21] Copyright 2022, Elsevier. e) Scheme of Shockley dislocation in the FCC structure.[26] f) High-angle annular dark-field scanning transmission electron microscopy (HAADF-STEM) of dislocation core on steel. Reproduced with permission.[28] Copyright 2017, Elsevier. g) Scheme of a twin in the FCC structure.[26] h) HAADF-STEM image of MnS with twin structures. Reproduced with permission.[29] Copyright 2014, Elsevier. a,c,e,g) Reproduced under the terms of Creative Commons Attribution 4.0 International License (https://creativecommons.org/licenses/by-nc-sa/4.0/deed.en).[26]

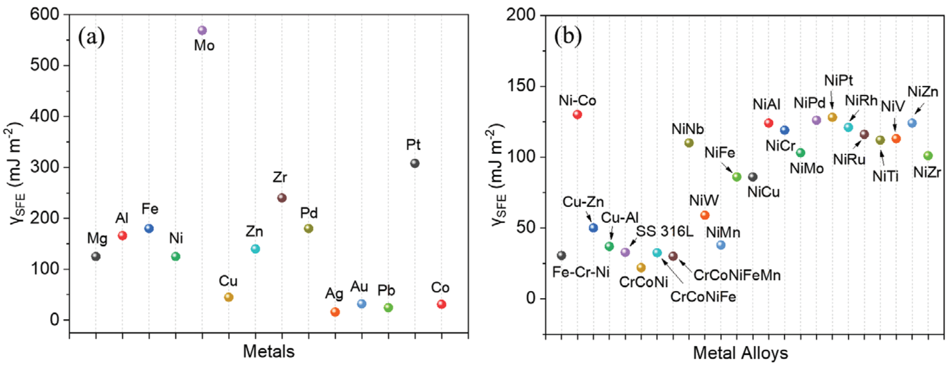

Figure 4. SFs energy (γ_{SFE}) of a) metals and b) metal alloys. Data collected from refs.[33]

or recrystallization. The resulting sequence becomes ABCABCACBACBA. This transformation in the stacking sequence leads to SF known as twinning (see Figure 3g,h).

1.3. Methods to Create SFs

Understanding the mechanisms driving SF formation is critical to enhance control over SF and, ultimately the ability to fine-tune the physical properties of nanomaterials through defect engineering. The SF energy (γ_{SFE}) is closely related to the occurrence of SF within the ground state of the crystal structure and is an important parameter for FCC metals, reflecting the ability of the crystal to respond to deformation.[30] SF is formed due to the dissociation of lattice dislocations into partial dislocations, a process aimed at minimizing elastic energy following Frank's rule.[31] The size of the SF region (i.e., the distance between partial dislocations) is determined by a delicate balance between the repulsive elastic interaction among the partial dislocations and the energy required to form the SF between them (termed γ_{SFE}). In FCC crystals, γ_{SFE} and, consequently, the dislocation dissociation width have a notable impact on dislocation mobility, the capacity for cross-slipping, and the occurrence of twinning. These factors collectively dictate the mechanical behavior of the crystal.[30,32] It is widely acknowledged that Ag possesses the lowest γ_{SFE} (16 mJ m^{-2}) among all elemental metals (**Figure** 4a), thus promoting the formation of SF. It is shown that the chemical changes introduced by alloying have an additional impact on the γ_{SFE} and therefore influence the mechanical response, as depicted in Figure 4b.[33] The methods for generating SF in metals and metal alloys are summarized as follows.

1.3.1. Annealing

Defect sites can be effectively created during solidification or phase transformation under various atmosphere conditions using calcination and annealing techniques effectively generates.[34] For example, the controlled adjustment of SF density in $\mathrm{Li_2MnO_3}$ perovskite was achieved through the calcination of MnO and an excess of 5% $\mathrm{Li_2CO_3}$ at 900 °C for 15 h in an oxygen–nitrogen mixture at different oxygen contents (20%, 40%, 60%, 80%, and 100%).[24b] This process resulted in the creation of distinct types of SFs, as illustrated in **Figure** 5a–c. The Z0 model represents a seamless, SF-free R-type configuration within the transition metal layers (Figure 5a,d). By initiating from Z0 without SFs, various SF modes in diverse models can be induced by displacing the transition metal layers, resulting in an R/P-type staggered configuration, referred to as Z1 (Figure 5b,e) and a seamless P-type configuration, denoted as Z2 (Figure 5c,f). The development of these SFs in the perovskite structure (as demonstrated in the HAADF-STEM image in Figure 5g) was directly associated with the oxygen partial pressure during the synthesis procedure and exhibited an increase with elevated oxygen partial pressure. The Li/Mn ordered arrangement within the $\mathrm{LiMn_2}$-layer was reflected in the X-ray diffraction (XRD) patterns of $\mathrm{Li_2MnO_3}$, where peaks associated with the superstructure emerged at 20°–34° (Figure 5h). The superstructure peaks exhibited broadening due to the presence of SFs. Employing a similar solid-state sintering method, $\mathrm{Li_2RuO_3}$ containing SF was synthesized by annealing $\mathrm{RuO_2}$ and $\mathrm{LiCO_3}$ with a 10% excess of Li at 900 °C for 12 h. Following this, a subsequent annealing step was conducted at 1000 °C for another 12 h.[35] Meng et al.[36] successfully prepared aluminum nitride nanowires (AIN NWs) containing SF through a thermal nitridation process. This process involved metal aluminum, and ammonium chloride and was carried out at 1000 °C and 1 atm pressure, with $\mathrm{N_2}$ and $\mathrm{H_2}$ as the co-flowing gases. Subsequently, the solids were left to cool naturally to room temperature in the presence of an $\mathrm{N_2}$ and $\mathrm{H_2}$ atmosphere. The presence of hydrogen played a pivotal role in facilitating the dislocation-driven growth mechanism. Their findings suggested that the partial dislocations and SF on the AIN NWs emerged primarily during the post-growth cooling phase, as opposed to the crystal growth process. Wang et al.[37] used a straightforward annealing method to induce defects in Ag nanowires (such as SFs, penta-twinned structure) through calcination in a tube furnace under $\mathrm{N_2}$ protection. They observed a clear correlation between defect density and annealing temperature. Specifically, they noted a significant reduction in defect densities of the Ag nanowires as the annealing temperature was raised from 180 to 300 and 500 °C.

1.3.2. Laser Ablation in Liquid (LAL)

Introducing defects into metallic crystals can be effectively achieved using the LAL strategy.[22a] This process involves rapidly

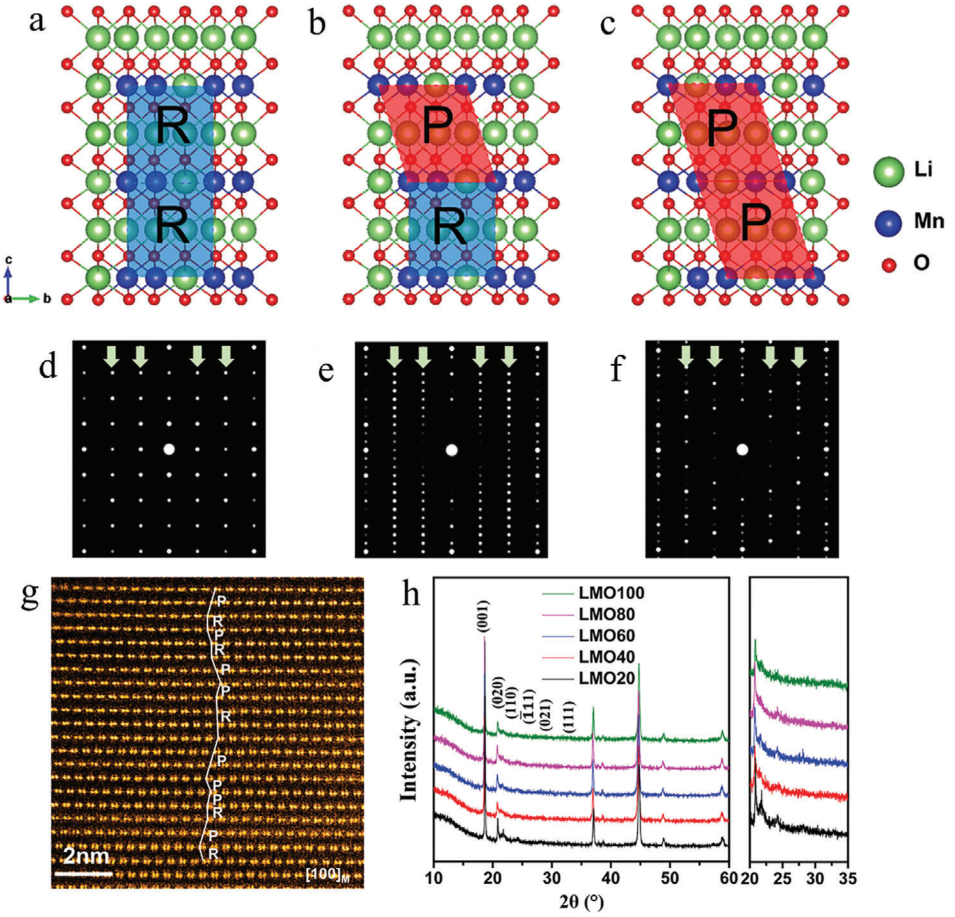

Figure 5. Schemes of a) Z0 stacking mode (Seamless R-type arrangement in Blue), b) Z1 stacking mode (R/P staggered arrangement in Blue and Red), and c) Z2 stacking mode (Seamless P-type arrangement in Red). The simulated electron diffraction patterns of d) Z0, e) Z1, and f) Z2. g) HAADF-STEM image of LMO100 (100% oxygen content atmosphere). h) XRD patterns of LMO series samples were achieved under atmospheres with oxygen content ranging from 20–100%. Reproduced with permission.[24b] Copyright 2023, Wiley.

heating a metallic target with a pulsed laser, forming high-temperature vapor and liquid droplets. Subsequently, these droplets undergo a cooling process facilitated by the surrounding liquid medium, resulting in the formation of nanoparticles. The rapid cooling process hinders atomic movement, leading to the retention of many defects. The rate at which the cooling process occurs is a key factor in defect formation. Kang et al.[22a] employed the LAL technique to synthesize Ag nanoparticles. They manipulated the liquid medium using liquid nitrogen (LN), ice water (IW), and boiling water (BW) to control the cooling rate. It was observed that the defect rates could be easily tuned by altering the properties of the liquid medium. More precisely, lower temperatures of the liquid medium led to higher defect rates: Ag-LN > Ag-IW > Ag-BW. Zhou et al.[38] achieved a large-scale synthesis of defective PtNi nanocatalysts, which were securely attached to a nickel foam (NF) substrate using a process of millisecond laser direct writing in liquid nitrogen (LN), employing a commercial laser welding machine (**Figure** 6a–c). This process resulted in high-density edge dislocations ($\approx 1013\ \mathrm{cm}^{-2}$) along various orientations within PtNi nanocrystals. In this technique, a millisecond laser was used to ablate a metal foil in a liquid medium, causing the forceful ejection of metal nano-droplets owing to a powerful shattering effect. These nano-droplets then quickly solidified and condensed onto the metal plate, forming arrays of metal nanoparticles. These nanoparticles were securely attached to the metal foil owing to the effects of quenching and confinement facilitated by LN. Applying the dislocation theory to bulk metals, it is known that the rapid solidification of molten metal can yield a large number of dislocations within the materials. When the dislocation lines intersect and create a network, they efficiently inhibit the movement of dislocations, thereby stabilizing them within the bulk metals (Figure 6d–g). Additional catalysts featuring SF were synthesized via laser direct writing strategy, exemplified by the Ag@NiO/NF[39] and Ag nanoparticles.[19] Additional catalysts featuring SF were synthesized via laser direct writing strategy, exemplified by the 3D branched Ni nanoparticles,[40] PtAgCo nanosheets,[16] Pt–Cu hierarchical quasi great dodecahedrons.[41]

1.3.3. Hydrothermal Synthesis

Hydrothermal synthesis is typically conducted within a closed system (e.g., Stainless steel outer container and Teflon inner container) under elevated temperatures and pressure conditions.

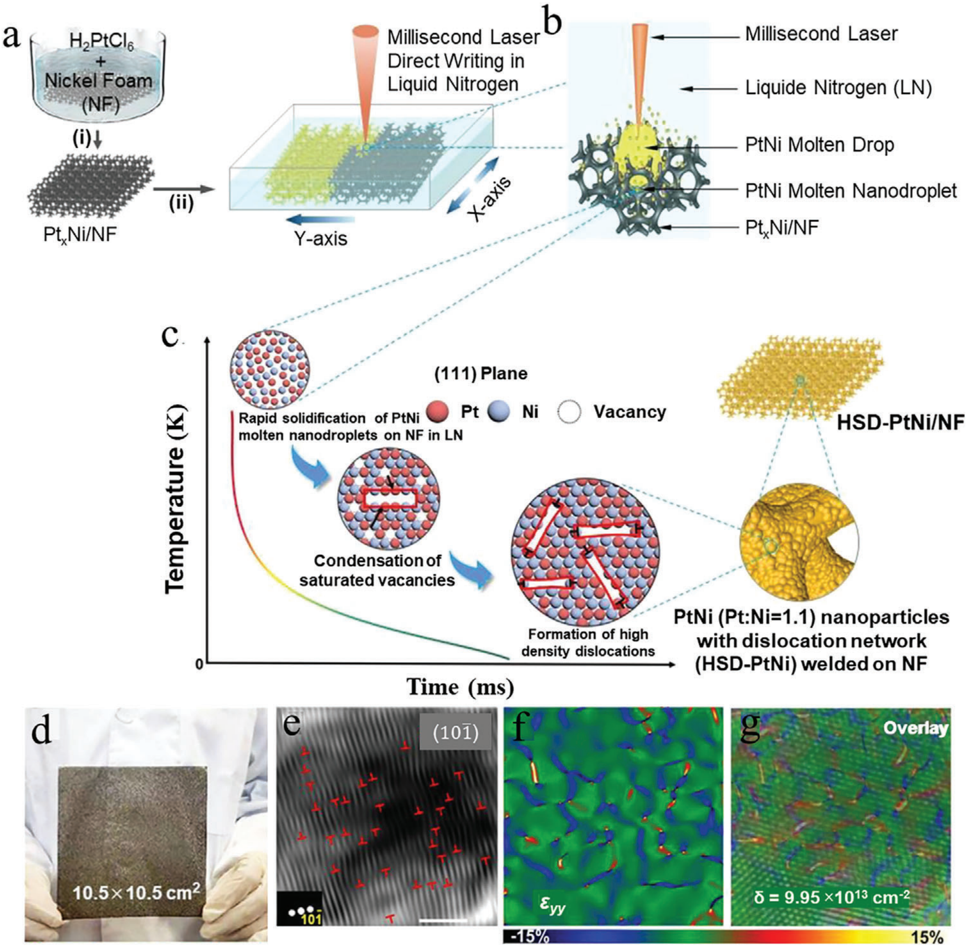

Figure 6. a) Scheme of the two-step synthesis of PtNi/NF electrode. Step (i) is to immerse NF in an H_2PtCl_6 solution to attain Pt_xNi/NF. Step (ii) is to perform millisecond laser direct writing treatment on Pt_xNi/NF in liquid nitrogen. b) Scheme showing how PtNi turns into molten nanodroplets and is sprayed and condensed on NF during millisecond laser direct writing. c) Illustration of hypothesized edge dislocation formation mechanism, because of quenching and confinement caused by LN, PtNi nanodroplets formed at high temperature rapidly condensed on the NF surface and formed edge dislocations. d) Photograph of the prepared PtNi/NF electrode with a large area. e) Inverse fast Fourier transformation (IFFT) image of PtNi/NF displayed edge dislocations, highlighted with red ⊥. f) Contour plot of the strain component ϵ_{yy} obtained through geometric phase analysis on (e). g) An overlay of strain components ϵ_{xx} and ϵ_{yy} superimposed onto the HRTEM image. Reproduced with permission.[38] Copyright 2022, Wiley.

This method offers several advantages, including precise crystal growth, the ability to control particle size, uniform distribution, minimal agglomeration, and the ease of adjusting stoichiometry and crystal morphology. By performing a one-step hydrothermal treatment of Ni foil and sulfur powder, nickel sulfide films with different morphologies (hierarchical dendrites, nanobelts, and nanorods) were grown on the Ni foil, which exhibited a significant presence of SFs.[42] Furthermore, employing the same hydrothermal treatment approach with respective metal foils and chalcogenides, the authors successfully synthesized a range of oriented nanostructured metal chalcogenides films (including Fe, Sn, and Cu). Zhang et al.[24c] used a typical hydrothermal strategy to prepare Mn modified $Ni(OH)_2$ on NF substrate. They observed a modification in the stacking pattern of layers correlated with the Mn doping level. The introduction of Mn^{4+} ions led to an increased accommodation of anions in the interlayers, which expanded the spacing along the *c*-axis direction. Additionally, the bond lengths of Ni—O and Ni-metal decreased, and the ab planes of NiO_2 slabs experienced contraction. The introduction of manganese atoms exclusively at 3a sites led to the development of a unique SF disorder that emerged within undoped-doped-undoped slabs, imparting structural stability during the battery cycling process.

1.3.4. Oxidative Etching

A standard process for direct nanocrystals synthesis encompasses three distinct stages: i) nucleation arising from the reduction of metal ions, ii) the transition from nuclei to seeds, and iii) the expansion of seeds into nanocrystals. Throughout these stages, oxidative etching assumes a pivotal role, sometimes exhibiting intricate and interconnected effects on each.[43] Pioneered by Xia's group, a gentle solution-phase approach utilizing polyol synthesis at temperatures below 200 °C, was developed to generate Ag nanowires with consistent diameters and large-scale

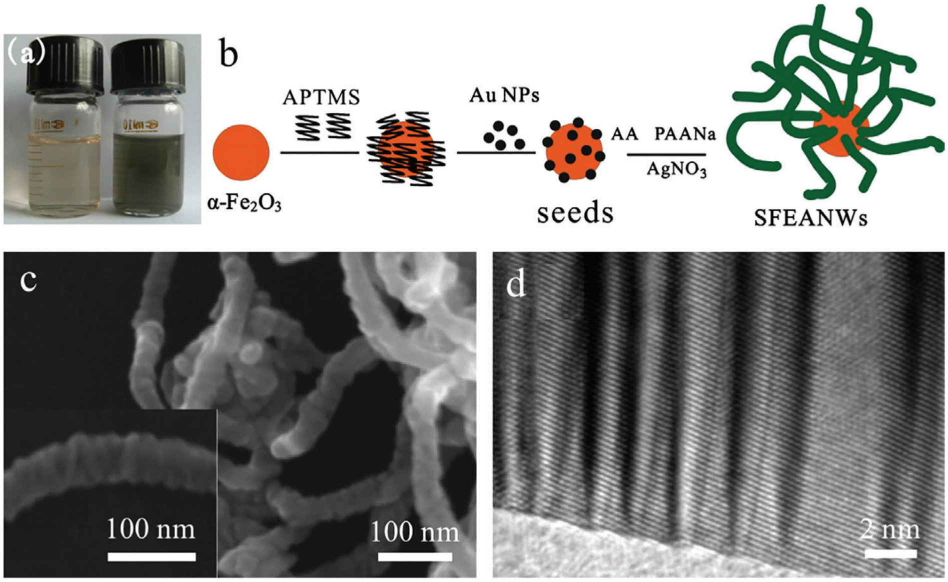

Figure 7. a) Photograph of dilute seeds solution on the left and the SFEANWs solution on the right, b) scheme of the synthetic process of SFEANWs, c) SEM images of SFEANWs, d) HRTEM of SFEANWs. Reproduced with permission.[46] Copyright 2013, Elsevier.

production efficiently. In this process, pre-prepared Pt nanoparticles acted as seeds, catalyzing the growth of Ag nanowires by reducing AgNO$_3$ with the assistance of ethylene glycol.[44] Further investigations by Wang et al.[45] revealed that by varying the choice of polyols and adjusting temperatures, it is possible to finely regulate the reduction rate in the polyol synthesis of noble metal nanocrystals. This control produced nanocrystals exhibiting specific twin structures, such as single crystals, multiple twins, and SF structures. Using Pd as an illustrative example, they established a clear quantitative relationship between the initial reduction rate and the stacking defect structure in the nanocrystals. This insight allowed for precisely synthesizing high-purity Pd nanocrystals with unique twin structures (such as single crystals, multiple twins, and SFs). Similarly, Xu et al.[46] employed α-Fe$_2$O$_3$/Au as a seed to catalyze the growth of Ag nanowires by reducing AgNO$_3$ using ascorbic acid with sodium polyacrylate (**Figure** 7a,b). This process successfully created numerous SFs on the Ag crystalline structure, denoted as SFs-enriched Ag nanowires (SFEANWs) (Figure 7c,d). In another study, Lu et al.[47] detailed the synthetic method for preparing ultrathin Au nanowires with rich SF using an oleylamine solution. They suggested that this structure with a high density of SF emerged from stacking blocks to form a wire with atomic steps, thereby generating inner stress and producing Shockley partial dislocations. Cu nanodisks featuring SF were formed within mixed reverse micelles, utilizing an excess of hydrazine as the reducing agent.[48] The several parallel SF on (111) planes served as catalyst sites for the nucleation, consequently expediting growth along the twin planes.

1.3.5. Electrochemical Method

The electrochemical synthesis of metal nanostructures (e.g., Ag) offers a distinct advantage over other methods, mainly due to its easily controllable electrochemical driving force, known as the overpotential. Studies have shown that manipulating this driving force for crystallization leads to diverse crystal morphologies, ranging from sharply faceted nanoparticles to intricate hierarchical structures such as dendrites and the induction of SF during crystal growth.[49] Hence, electrodeposition is a potent processing approach that provides the flexibility to tailor metal architectures at the micro/nanoscale. The mechanisms of electrochemical synthesis of SF can be mainly divided into two categories: i) Voltage or Current Pulse Method: by employing the voltage or current pulse method in electrochemical deposition, the driving force for crystallization can be altered rapidly and periodically. This results in the formation of planar faults by either removing one or more atomic layers or inserting one or more extra layers into a perfect crystal lattice generated through potentiostatic or galvanostatic deposition. ii) Selective Removal of Non-Metal Atoms: another approach involves selectively removing non-metal atoms in metal compounds (e.g., oxides, sulfides, and nitrides) under reductive potentials. This leads to the formation of nonstoichiometric metal-dominant compounds, generating various lattice defects, including SFs, during the accommodation of nonstoichiometry. Radmilović et al.[49] synthesized Ag dendrites with abundant SFs and twins aligned parallel to the ⟨111⟩ broad dendrite surface (**Figure** 8a–d). SFs and twins acted as sites for heterogeneous nucleation, thereby promoting dendrite growth through a ledge growth-assisted mechanism. In another study, an Ag/graphene composite featuring controllable SF density was fabricated through an electrochemical reduction process.[50] In this method, Ag was electrodeposited onto a piece of graphite paper, employing a current-pulse mode with a peak current density of 1 A cm^{-2} in a standard two-electrode cell, using a silver foil as the anode, and 1 M AgNO$_3$ as the electrolyte. Fang et al.[51] conducted treatments on the copper foam (CF), employing thermal exposure in air and a chemical solution method. These treatments resulted in two distinct phases:

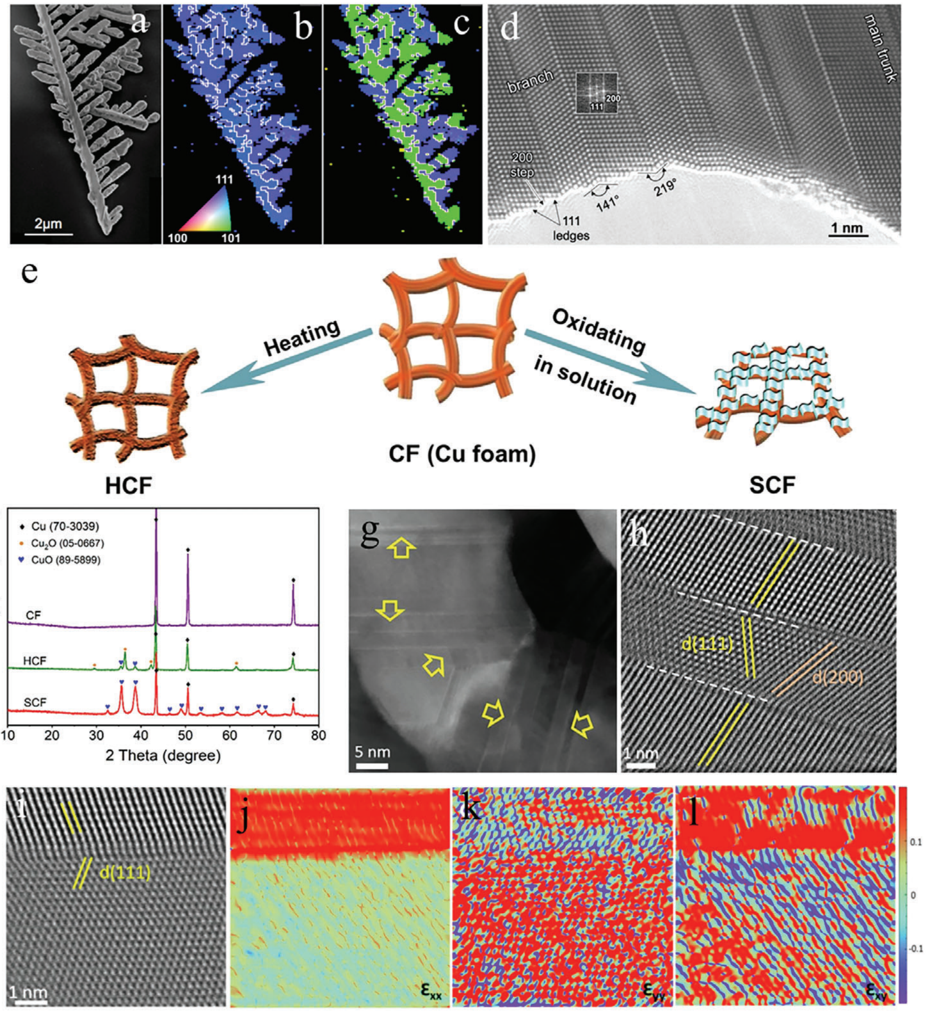

Figure 8. a) SEM of an Ag dendrite recorded after FIB polishing. b) Orientation map, the stereographic triangle exhibits the crystal orientation of the dendrite, and the white lines show the twinning boundaries. c) Orientation imaging color-coded map indicating two twinning variants. Reproduced with permission.[49] Copyright 2016, American Chemical Society. d) HRTEM image displaying Ag twins located in the region between the dendrite trunk and branch. e) The synthetic diagram of Cu electrodes: HCF and SCF. f) XRD patterns of CF, HCF, and SCF, g–l) HAADF-STEM images of SCF following 120 min of the electrocatalytic NO_3RR. Reproduced with permission.[51] Copyright 2022, Elsevier.

heterogeneous Cu_2O/Cu foam (HCF, Cu transformed to Cu_2O) and superconducting CuO/Cu foam (SCF, Cu transformed to CuO), as illustrated in Figure 8e,f. Specifically, the SCF was prepared by immersing CF in a mixed solution comprising NaOH and $(NH_4)_2S_2O_8$ at 60 °C. Remarkably, during the electrocatalytic NO_3RR employing SCF as the electrocatalyst, a notable density of SF emerged (Figure 8g–l). They observed that under the applied reduced potential of −1.3 V versus SCE (SCE: saturated calomel electrode) in NO_3RR, Cu-based oxides experienced a loss of structural oxygen ions, resulting in nonstoichiometry. Consequently, the applied negative potential might induce the formation of defects to adapt this nonstoichiometry.

1.3.6. Other Methods

Zhang et al.[52] applied a simple heat and cool shock calcination strategy to induce defects (stack faults, twin boundaries, lattice distortion, surface steps), refine grains into Ni, and regulate the defect rates by fine-tuning the heating and cooling methods and calcination time. A similar thermal-shock heating method was employed to synthesize SF-featured Ru nanoparticles.[21a] Additionally, as depicted in **Figure 9**a, another pioneering endeavor employed a cation exchange reaction strategy to replace the Cu^+ cations within roxbyite $Cu_{1.8}S$ nanorods (Figure 9b) with Zn^{2+} ions, yielding ZnS nanorods (Figure 9c). This process engendered a notable proliferation of SFs.[53] In the course of the cation exchange process, significant shifts occurred in the stacking sequence of the closely-packed anion sublattice at multiple points, resulting in the formation of a nanorod exhibiting a composite crystalline structure comprising wurtzite (wz), zincblende (zb), and a wz/zb polytype. Each structure encompassed an organized sequence of SF (Figure 9d). Moreover, the reaction temperature played a crucial role in governing the cation exchange rate, acting as a synthetic lever that finely modulated the SF density, ranging from high to low, as illustrated in Figure 9e–g. The synthe-

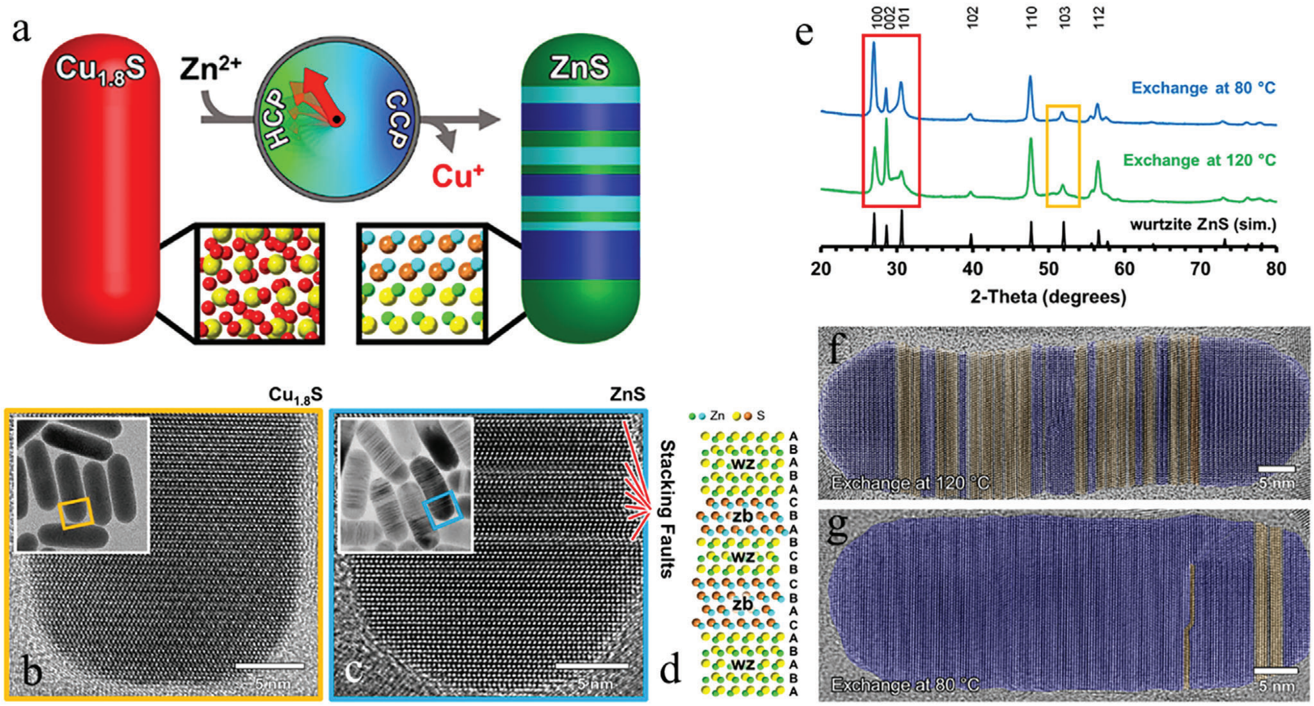

Figure 9. a) Scheme of phase transfer from $Cu_{1.8}S$ to ZnS with SF through cation exchange reactions. TEM (insert) and HRTEM images of b) $Cu_{1.8}S$ precursor nanorods and c) ZnS nanorods. d) The atomic model of SF formed because of the transition from wz to zb layers. e) XRD profiles of ZnS nanorods prepared at temperatures of 80 and 120 °C. False-color HRTEM images f) ZnS nanorods at 120 °C and g) ZnS nanorods at 80 °C, the blue color represents wz while the yellow color represents zb layers. Reproduced with permission.[53] Copyright 2021, American Chemical Society.

sis of defective $Ni_{30}Mo_{70}$, $Co_{30}Mo_{70}$, $Co_{30}Ni_{70}$, and $Co_{10}Ni_{20}Mo_{70}$ alloy electrodes with SF structure was obtained through a ball milling approach. This involved milling the designated quantities of bulk metallic powders comprising Ni, Co, and Mo under an argon atmosphere.[54] SF can also arise through a chemical leaching process. For instance, Su et al.[55] conducted a high-temperature $NaBH_4$ leaching treatment on $BaTiO_3$ nanoparticles, by treating a mixture of 0.1 g as-synthesized porous $BaTiO_3$ nanoparticles and 0.2 g $NaBH_4$ in a cylindrical electric furnace at 400 °C under pure Ar for 2 h. In this reaction, the Lewis base H^-, released from $NaBH_4$ under elevated temperatures, found it more accessible to acquire oxygen from the TiO_2 plane compared to the BaO plane. Consequently, the ABAB stacking sequence (with A representing the BaO plane and B representing the TiO_2 plane) in the local surface layer of $BaTiO_3$ is disrupted, creating SF structures.

1.4. Characterization Techniques for SFs

Several techniques can be used to characterize SFs in materials. It is important to note that no single technique may be sufficient, and often, a combination of these methods, along with careful sample preparation and analysis, is used to characterize SFs in materials accurately. The choice of techniques depends on the specific material, the nature of the SFs, and the desired level of detail in the characterization. The capabilities, advantages, and limitations of various characterization techniques for SFs in materials are summarized in **Table 1**.

- HRTEM: HRTEM provides atomic-scale imaging, allowing direct visualization of SFs and their arrangement within the crystal lattice. SF appears as areas of disrupted atomic arrangement.
- Selected Area Electron Diffraction (SAED): SAED involves exposing a small sample area to a focused electron beam and analyzing the resulting diffraction pattern. SAED patterns in TEM can reveal the presence of SFs by showing extra diffraction spots or streaks with altered diffraction patterns.
- STEM: STEM uses a focused electron beam to scan across a sample. Detectors collect signals, allowing for imaging and spectroscopic analysis of individual atoms. STEM and techniques like annular dark-field imaging can provide detailed information about the crystal structure and defects like SFs.
- XRD: XRD can be used to study materials' crystallographic structure, including SFs. Discrepancies in peak positions and intensities, along with peak broadening, serve as indicators for the presence of SF.
- X-ray Photoelectron Spectroscopy (XPS): XPS can be used to analyze a material's chemical composition and electronic states, which can indirectly provide information about SFs. Shifts in binding energies or peak shapes can indicate SFs.
- X-ray absorption spectroscopy (XAS): XAS stands out as a powerful technique for exploring electronic structures, lattice strains, and coordination configuration of materials with SFs. The rising edge of X-ray absorption near-edge structure (XANES) reflects the valence state of the specific element. Fourier transform extended X-ray adsorption fine-structure

© 2024 The Authors. Advanced Materials published by Wiley-VCH GmbH

Table 1. Summary of characterization techniques for SFs in materials.

Techniques	Capabilities	Advantages	Limitations
HRTEM	Nanometer-scale analysis and atomic-level details of SFs	Direct visualization, high resolution	Thin samples, noise sensitivity, beam damage, limited field of view
SAED	Diffraction pattern of a small sample area by a focused electron beam	Extra diffraction spots or streaks indicate SFs	Thin samples, limited by selected area and orientation
STEM	Scanning across a sample by a focused electron beam and collecting signals	Detailed information about structure and defects	Thin samples, noise sensitivity
XRD	Crystallographic structure by diffraction of X-rays	Peak discrepancies indicate SFs	No direct visualization, insensitive to small or localized defects
XPS	Chemical composition and electronic states by emitted electrons after X-ray irradiation	Binding energy or peak shape shifts indicate SFs	No direct visualization, not specific to SFs
XAS	Chemical composition, coordination configuration, and electronic structure	High sensitivity to detect low CNs, indicating defects	Limited access and high cost of synchrotron facilities, beam-induced sample damage
Raman Spectroscopy	Crystal structure and symmetry by scattered light after laser irradiation	Peak changes in the Raman spectrum suggest SFs	No direct visualization, not specific to SFs
AFM	Surface morphology and topography by interaction force between a probe and the sample	Surface irregularities may be associated with SFs	No direct visualization, insensitive to subsurface or bulk defects
STM	Atomic-scale images of surfaces by tunneling current between a probe and the sample	Reveal defects, including SFs, on the surface	No direct visualization, insensitive to subsurface or bulk defects
PAS	The density of defects by the annihilation of positrons and electrons	Positron annihilation signal changes indicate defects, including SFs	No direct visualization, not specific to SFs
AES	Surface composition by emitted electrons after electron irradiation	Auger spectra changes may indicate SFs	No direct visualization, not specific to SFs
Computer Simulations and Modeling	Prediction and understanding of SFs by theoretical calculations and computer simulations	Insights into the formation and behavior of SFs complement experimental techniques	No direct visualization, may not be accurate or realistic, high computational power

(FT-EXAFS) can be employed to study the detailed coordination configuration of catalysts, including coordination number (CN) and bond length, which furthermore reflects the properties of defects like SFs.

- Raman Spectroscopy: Raman spectroscopy can provide insights into a material's crystal structure and symmetry. SFs can influence the Raman spectra. Changes in peak positions or intensities in the Raman spectrum can suggest SFs.
- Atomic Force Microscopy (AFM): AFM can be used to study the surface morphology and topographical information of materials, and in some cases, it can reveal surface irregularities that may be associated with SFs.
- Scanning Tunneling Microscopy (STM): STM can provide atomic-scale images of surfaces, potentially revealing defects, including SFs.
- Positron Annihilation Spectroscopy (PAS): PAS can provide information about the density of defects in a material, including SFs. Changes in the positron annihilation signal can indicate the presence of defects, including SFs.
- Auger Electron Spectroscopy (AES): AES can be used to analyze the surface composition of a material, which can indirectly provide information about SFs. Changes in Auger spectra may indicate the presence of SFs.
- Computer Simulations and Modeling: Theoretical calculations and computer simulations can be used to predict and understand the presence and properties of SFs in materials.

SF profoundly influences various material characteristics, including conductivity and mechanical properties. Notably, they play a pivotal role in shaping catalytic behavior. This arises from the fact that atoms on the SF surface exhibit reduced CN and substantial lattice strain, all of which are crucial for regulating the properties of active sites responsible for adsorbing reactants and intermediates. In the following sections, we have discussed the correlation between SF and catalytic efficacy concerning reactions for hydrogen production, such as HER, OER, overall water splitting, and additional electrocatalytic reactions like ORR, NO_3RR, and energy storage.

2. SFs-Based Catalysts for HER

2.1. Electrocatalytic HER

Electrocatalytic HER is an electrochemical process where hydrogen can be produced from either water or proton with the assistance of cathodic potentials. As summarized in the previous section, the productivity of HER is highly related to the adsorption/desorption of reaction intermediates such as *H. Based on the Sabatier principle, an ideal electrocatalyst for HER should neither strongly nor weakly bind H. Under this circumstance, the adsorbed *H species can be easily generated and combined with another *H species or $H^+ + e-$ to form an H_2 molecule easily. By introducing proper SFs into electrocatalysts, the electronic structure of the pristine active site could be efficiently modulated.

Compared to another defect, vacancy, which is commonly studied in various catalytic processes, SFs have several advantages in fabricating high-performance HER catalysts. i) Vacancy suffers from low stability under reductive potentials, while SFs can remain very stable and almost unchanged under reductive potentials for HER. This could contribute to good structural and catalytic stability of SF-engineering electrocatalysts. ii) SFs could be considerably larger due to their much more ordered configuration compared to the small population (10^{-8} to 10^{-4}) of disordered vacancies in electrocatalysts. This could bring the SF modulation strategy much more potential in tuning HER adsorption energy and catalytic performances.

As one of the most popular 2D materials, MoS_2-based materials have weak Van der Waal's combination between layers. Therefore, their SF energy is also significantly lower than that of other metal compounds, making introducing SFs into Mo-based catalysts relatively easier. By treating commercial MoS_2 with high pressure (1, 3, or 5 GPa), abundant SFs were formed from surface shear strain, which could not only modify the original poor electric transport in the *c*-axis but also activate the inert basal plane of MoS_2.[17b] Therefore, the overpotential at 10 mA cm^{-2} was improved from 536 to 452 mV for the MoS_2-3-200 catalyst (treated under 3 GPa pressure and 200 °C). Additionally, the good catalytic stability of MoS_2-3-200 was also verified by the stable current density observed throughout 15 h and nearly unchanged polarization curves even after 2000 cycles.

In the carbon shell encapsulated MoP catalyst,[56] SFs were evidenced by the HRTEM image (**Figure** 10a–f) and the corresponding interlaced diffraction line of the SAED image (Figure 10d). Because high-temperature synthesis will convert SF to lattice defects, MoP-800 hasmore active sites for HER than MoP-1000, which was verified by the larger electrochemical surface area (209. 25 vs 101.25 cm^{-2}) (Figure 10c). Density functional theory (DFT) calculation found that the intrinsic electrocatalytic activity of MoP was improved with the addition of SF defects and carbon layer (Figure 10h–m). The combined impact of the defect and carbon shell on the electronic structure collaboratively enhances water adsorption strength and fine-tunes the adsorption-free energy of hydrogen. This collaborative effect contributes to an improved performance in the HER under alkaline conditions. In addition to directly modulating the adsorption energy of *H or increasing the active sites, SFs can also induce other structure defects, realizing the indirect contribution to the improved HER performances. Zeng and co-workers[41] synthesized novel Pt–Cu hierarchical quasi-great dodecahedrons (HQGDs) by growing hierarchical high-order Cu branches on icosahedral Pt seeds. The Pt–Cu had a typical dodecahedron structure from different orientations. The dodecahedron structure involves 12 pentagons, five of which meet at the vertex and intersect with each other to form a pentagrammic path. The {111} twin plane was due to Cu's much lower SF energy than that of Pt (41 vs 330 mJ cm^{-2}). In addition to the apparent alloy effect and hierarchical frame structure, the unique twin defects that resulted from SFs also significantly improve the catalytic performance of HER by changing the strain effect and electronic structure of surface active sites. As a result, when compared to Pt–Cu hierarchical trigonal bipyramid nanoframes and commercial Pt/C catalysts, higher current density up to 316 mA cm^{-2} at the potential of −0.3 V and lower Tafel slope of 29.5 mV dec^{-1} can be recorded for Pt–Cu HQGDs. The excellent durability of Pt–Cu HQGDs was evidenced by the negligible decay (less than 1%) in current density after 5000 cycles and the sustained overpotential under a constant current density of 500 mA cm^{-2} for 10 h.

As discussed above, many studies have reported significantly improved HER performance by introducing SFs into various catalysts. Li et al.[19] systematically studied how SFs influence the fundamentals of the HER process through synthesizing Ag nanoparticles with low CN and large tensile strain. With the assistance of laser ablation in liquid strategy, abundant vacancies were generated in L-Ag, which tend to cluster on the close-packed Ag (111) planes before undergoing a collapse, leading to the formation of SFs. The SFs could be clearly distinguished from the HRTEM image. Moreover, 5.7% tensile strain was also calculated from Rietveld refinement of the XRD for L-Ag. Geometric-phase analysis was further carried out to study the distribution and extent of lattice strain. In Du's research,[19] the aligned strain and SFs were confirmed by a contour plot of sheer strain. In addition to the tensile strain, SFs were able to lower the CN of the L-Ag catalyst significantly. Specifically, the average CN value of L-Ag can be simulated to be ≈8.37, which is lower than those of Ag foil (≈12), S-Ag (≈11.1), and T-Ag (≈10.52). Then, the dependence of hydrogen adsorption-free energy ΔG_{H*} on the two parameters, CN and the tensile strain was calculated by the DFT method. It is concluded that low CN and large tensile strain could contribute to a lower ΔG_{H*} value, which according to the Sabatier principle, favors the generation and release of the H_2 molecule. When CN = 5 on the 8% strain (111) plane of the Ag catalyst, an extremely low hydrogen adsorption energy of 0.0007 eV was achieved by calculation, showing the great potential of the as-prepared L-Ag catalyst for HER. As expected, L-Ag did exhibit excellent catalytic HER performances. When compared to other Ag catalysts and commercial Pt/C, the lowest onset potential (6 and 32 mV at 1 and 10 mA cm^{-2}) and Tafel slope (31 mV dec^{-1}) agreed well with the theoretical prediction and strongly demonstrated the impressive HER activity of L-Ag. Moreover, a current density of 485 mA cm^{-2} can be recorded at −0.3 V versus reversible hydrogen electrode (RHE), which is 1.7 times higher than that of Pt/C (282 mA cm^{-2}). Due to the robust stability of the SF, the L-Ag polarization curve exhibited no noticeable shift even after 5000 cycles of testing. This suggests the significantly enhanced durability of L-Ag in comparison to commercial Pt/C catalysts. Similar SFs-rich Ag NPs can also be incorporated with Ni nanosheets on Ni foam through the so-called laser direct writing method.[57] Although the excellent HER performances, including low overpotential (167 and 180 mV at 1.0 and 1.5 A cm^{-2}) and robust stability (negligible activity decay after 120 h) were attributed to the coherent Ag(S)/NiO interfacial electronic coupling and strong chemical bonding between NiO and Ni foam. The existence of SFs in Ag(S) also slightly reduced the HER overpotential by ≈15 mV at 500 and 1000 mA cm^{-2}.

Compared with solely existing SF defects, it is more common that SFs co-exist with many other structural defects, including twin boundaries, stepped edges, and so on, which co-contribute to the overall HER activity enhancement. Therefore, a defect-rich molybdenum nitride/nickel anchored on carbon matrix (MoN/Ni@C) as shown in **Figure** 11a was successfully synthesized through a step-by-step method.[58] As shown in Figure 11b–e, various lattice defects, including twin

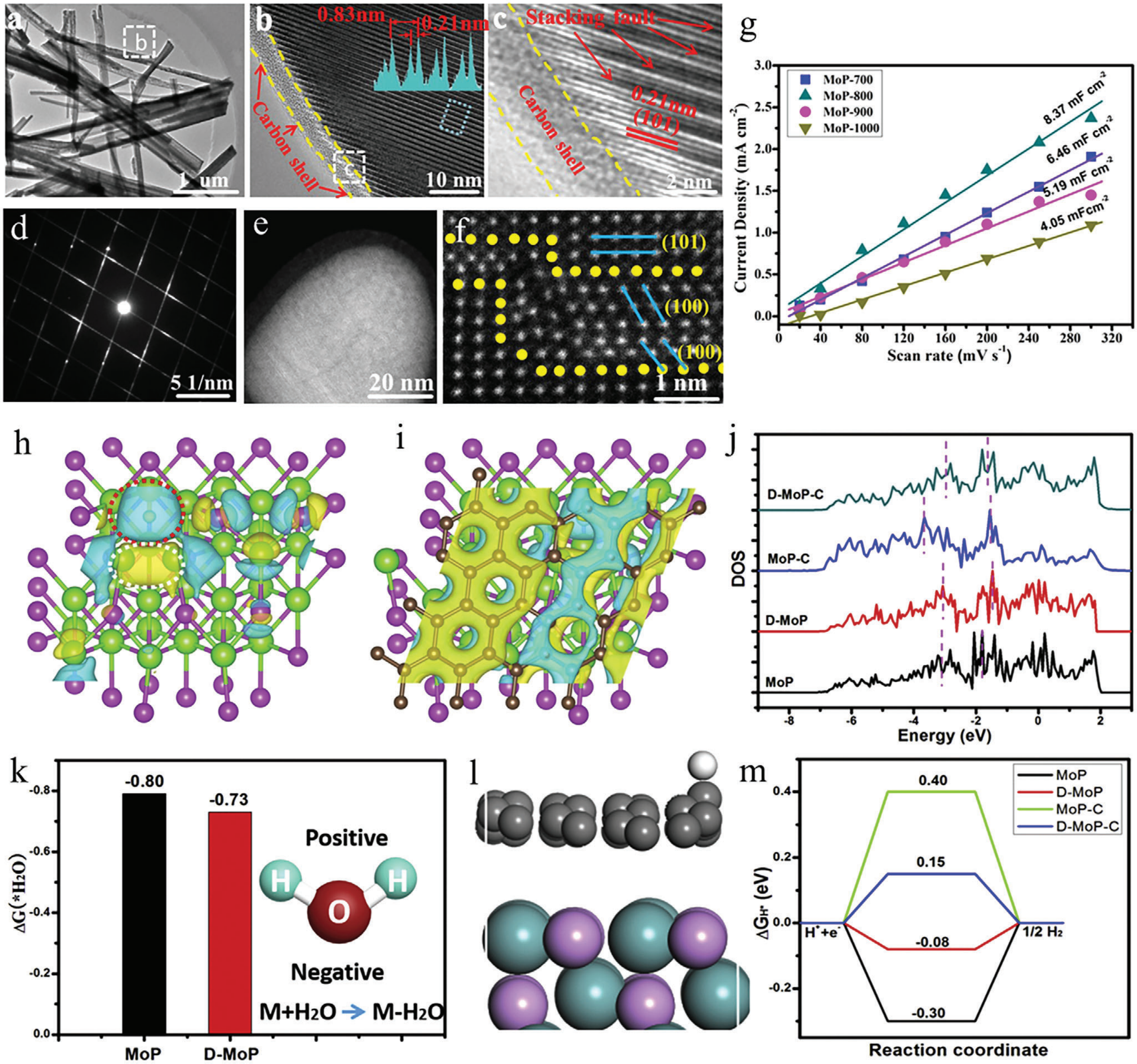

Figure 10. a,e) TEM, b,c,f) HRTEM, d) corresponding SAED image of MoP-800 with rich SFs. g) Plots of the current density at 0.20 V versus scan rate for the MoP-700, MoP-800, MoP-900, and MoP-1000. The electron-density-difference contour plot of defective MoP(101) h) without carbon coating and i) with carbon coating. The blue section represented a negative electron cloud, while the yellow section represented a positive electron cloud. j) The energy density of different sites on the MoP(101) surface. D: defective, C: with carbon coating. k) The free energy of water on defective and defect-free MoP(101) surface sites. l) The side-view of the proton adsorption structure on the carbon layer. m) The free-energy plot of HER on different sites of MoP(101) surface. Reproduced with permission.[56] Copyright 2021, Elsevier.

boundaries, stepped edges, and SFs, could co-exist in an as-prepared MoN/Ni@C catalyst. The abundant nanopores of Ni NPs could expose more active sites, while the stepped edges and SFs were beneficial for decreasing the adsorption energy of *H and later H_2 desorption. Moreover, the amorphous MoN could further generate more unsaturated sites and facilitate electron transfer. Reasonably, superior catalytic performance was achieved on MnN/Ni@C when compared to Ni@C, NF, and commercial Pt/C. The small overpotential of 27 mV at 10 mA cm^{-2} (Figure 11f) and low Tafel slope of 73 mV dec^{-1} (Figure 11g) evidenced the favorable HER thermodynamics and reaction kinetics. These impressive performances could be attributed to the abundant lattice defects mentioned above (including SFs), which promoted the adsorption of *H during the proton-coupled electron transfer step (PCET). The Nyquist plot also demonstrated charge transfer resistance comparable to that of Pt/C, further confirming the fast reaction kinetics on lattice defects of MoN sites. It is speculated that under an alkaline electrolyte, the Mo

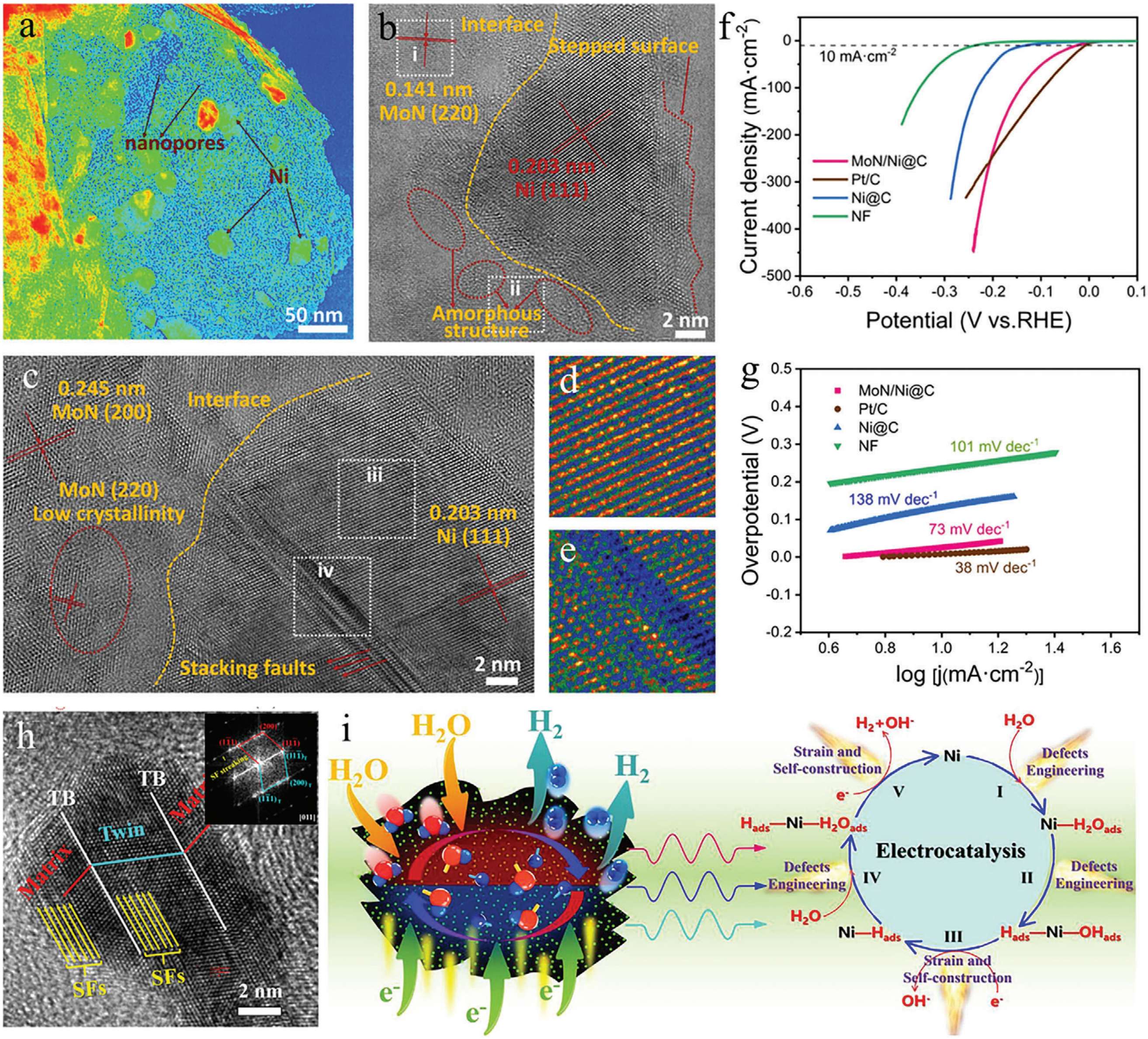

Figure 11. a) Thermal-colored TEM image of MoN/Ni@C. b,c) TEM images of MoN/Ni@C. Enlarged colored HRTEM images of d) area (iii) and e) area (iv) in (c). f) HER polarization curves and g) Tafel plots of the catalysts in 1.0 M KOH. Reproduced with permission.[58] Copyright 2023, Elsevier. h) HRTEM image of Ni-5-R, insert is FFT image along [011] direction. i) Illustration of hydrogen evolution on Ni-5-R catalyst and proposed mechanism of HER in alkaline on defective Ni-5-R. Reproduced with permission.[52] Copyright 2021, Elsevier.

ions tend to be oxidized to form soluble MoO_4^{2-}, leaving abundant defect sites on the catalysts. This could explain the excellent catalytic stability of Ni/MoN@C, where no distinct potential decay can be found after a continuous 180 h chronopotentiometry test. Song's group[52] developed a homemade tubular furnace with a rapid heating and cooling rate, which was used to synthesize Ni NPs cross-linked carbon sheets (Ni-5-R) with abundant twin boundaries and SFs. As can be seen from the HRTEM and corresponding fast Fourier transform (FFT) plot (Figure 11h), mirrored orientation along {111} crystal plane could be clearly distinguished under <011> axis, while $(11\bar{1})$ twin boundaries (TB) and SF were marked as white and yellow lines, respectively. Furthermore, the geometric phase analysis image again verified the existence of abundant strain due to lattice distortion, which preferentially distributes along the interface of TBs and SFs. As expected, compared to Ni-5-N which is prepared via a normal heating and cooling process, Ni-5-R showed an impressive onset potential of −0.0305 V and a much smaller overpotential of 68 mV at a current density of 10 mA cm^{-2}. The apparent performance enhancement can be attributed to the aforementioned abundant twin boundaries and SFs, which offer more active sites and optimize the adsorption of the reaction intermediate *H (Figure 11i). Moreover, good current density retention of ≈90% can be achieved after a 20 h potentiostatic test, verifying the good

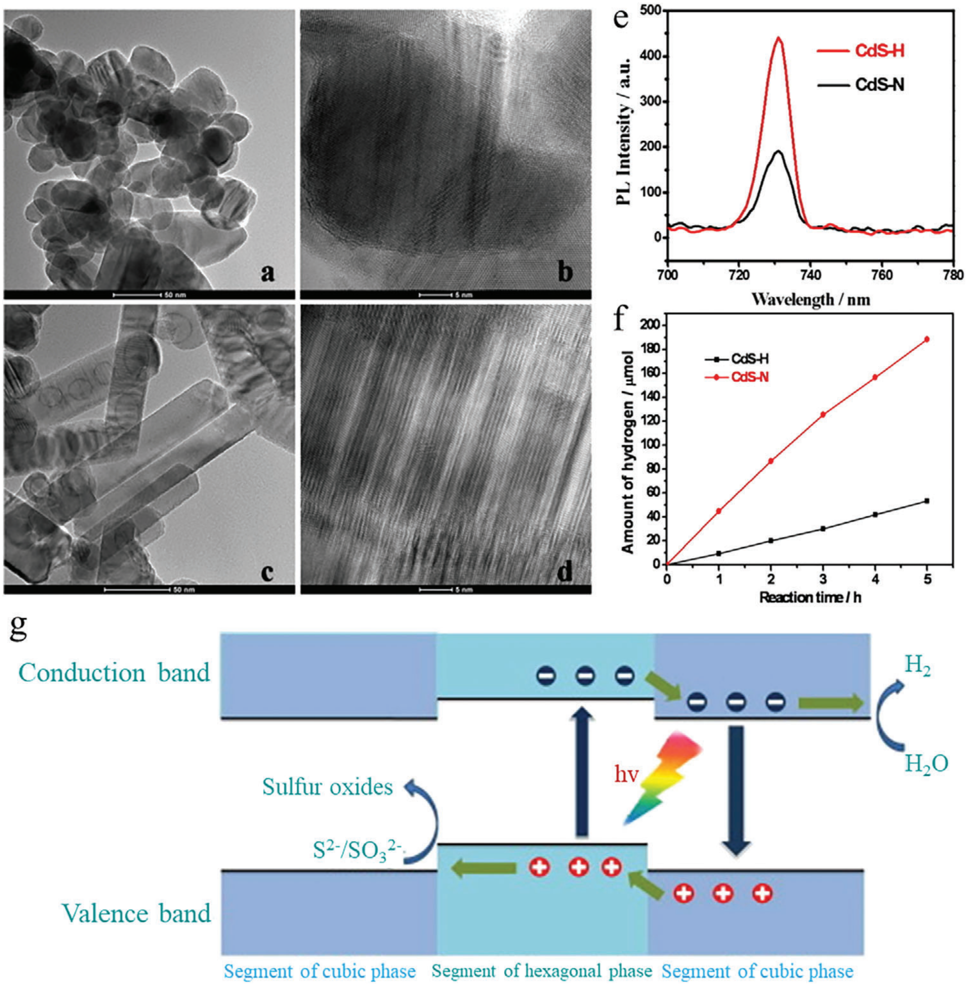

Figure 12. TEM images of a,b) CdS-H nanorod (deionized water as a solvent during hydrothermal synthesis) and c,d) CdS-N (ammonia as a solvent during hydrothermal synthesis). e) Photoluminescence spectra of CdS-N and CdS-H. f) Photocatalytic hydrogen production versus reaction time for CdS-N and CdS-H. g) Illustration of charge separation at the interface of hexagonal and cubic phase in the CdS-N with SF structure. Reproduced with permission.[59] Copyright 2015, Elsevier.

structural stability of twin boundaries and SFs in the Ni-5-R catalyst.

2.2. Photocatalytic HER

Using a semiconductor as an efficient photocatalyst, photocatalytic HER is a promising approach for directly generating green hydrogen from solar energy and water. Metal sulfides, particularly CdS, which demonstrate an exceptional response to visible light, possess a narrower band gap, a negative conduction band (CB) potential, and display high photocatalytic activity with the presence of sacrificial agents (e.g., Na_2SO_3/Na_2S). For example, by adjusting the hydrogen thermal reaction temperatures in concentrated ammonia solvent, CdS nanorods with different SF rates were synthesized (**Figure** 12a–d).[59] In the presence of engineered SF in CdS nanorods, electrons initially get excited from the valence band of hexagonal CdS to its CB when illuminated. They then migrate to the CB of cubic CdS for the HER. Simultaneously, photogenerated holes accumulate on the valence band of hexagonal CdS for oxidative reactions due to the terraced band. Consequently, the efficiency of separating electrons and holes created through photoexcitation is substantially enhanced in the SF region (Figure 12e). The photocatalytic H_2 production activity of the CdS-N nanorods catalyst with abundant SF showed a great improvement compared with CdS-H with a lower density of SF (Figure 12e). Due to distinct band structures observed in the cubic and hexagonal phases of CdS (illustrated in Figure 12g), a nanoscale terraced band structure may emerge between these phases. As a result, upon illumination of engineered CdS nanorods with SFs, electrons initially excited from the valence band of hexagonal CdS may transition to its CB and subsequently move to the CB of cubic CdS, facilitating the HER. Simultaneously, the terraced band structure encourages the aggregation of photogenerated holes on the valence band of hexagonal CdS, promoting oxidative reactions. This arrangement significantly enhances the separation efficiency of photogenerated electrons and holes at the SF region. The SFs and twins defects were observed when the phase transformation of CdS occurred from cubic to hexagonal during the hydrothermal process in the Na_3PO_4 solution.[60] The concentration of PO_4^{2-} affected the phase transfer efficiency and thus SF generation, a higher concentration led to more SFs and better photocatalytic activity of HER. He et al.[61] synthesized NiS-promoted CdS pyramids with SF defects by hydrothermal reaction in ammonia solution. The resulting NiS-CdS exhibited a high apparent hydrogen quantum yield of 49.2 mmol g^{-1} h^{-1} under visible light illumination. The p-type NiS and n-type CdS formed p–n junctions, and the unique SF structures improved the photo-carriers separation, contributing to the significantly enhanced photocatalytic activity for HER.

Besides, Zn-doped CdS catalysts exhibit improved photocatalytic performance toward HER. For example, Liu et al.[62] synthesized twin-induced 1D $Cd_{0.5}Zn_{0.5}S$ nanorod homo-junctions, which achieved excellent photocatalytic HER: 2.58 mmol h^{-1} g^{-1} of hydrogen generation rate and 62% of quantum efficiency of solar HER. The periodically occurred twin planes in $Cd_{0.5}Zn_{0.5}S$ nanorod resulted in the formation of alternating wurtzite (WZ) and zinc-blende (ZB) segments along the <111> direction. Compared to the ZB segments, the upward shift in the CB and valence band energy levels for the WZ segment facilitates the practical separation of photo-excited electrons and holes. The improved efficiency in photo-generated charge separation of twinning $Cd_{0.5}Zn_{0.5}S$ nanorod was identified as the domain factor for excellent photocatalytic hydrogen production. Another Zn-doped CdS photocatalyst ($Cd_{0.5}Zn_{0.5}S$(en)) with rich SF defects was developed, which exhibited a high photocatalytic hydrogen generation rate of 13.54 mmol h^{-1} g^{-1}.[63] The further modification with 0.25 wt.% NiS loading showed an H_2 production rate of 38.19 mmol h^{-1} g^{-1}. The nanosized NiS anchored on the SFs-rich $Cd_{0.5}Zn_{0.5}S$(en) generated a highly active interface, serving as sites for trapping electrons and contributing to suppressing the recombination of electron–hole pairs spatially. In addition, Gong et al.[64] combined the SFs-rich $Cd_{0.5}Zn_{0.5}S$ with Cu^{2+} incorporated carbon nanotubes (CNTs) to form a $Cd_{0.5}Zn_{0.5}S$-CNTs (Cu) catalyst. The Cu^{2+} anchored in the interface of $Cd_{0.5}Zn_{0.5}S$ and CNTs optimize the pathway for photogenerated electron transfer, while the CNTs suppressed the electron–hole recombination. The creation of SFs and, particularly, twins within the semiconductor serves a dual purpose: it prevents the photo-generated carriers from random scattering and hinders electron–hole recombination. All contributed to the excellent photocatalytic HER with an H_2 generation rate of 2.99 mmol h^{-1} g^{-1}.

Silicon carbide (SiC) has been recognized as a promising catalyst for efficient photocatalytic HER under visible light radiation. Its advantages include proper band gap (2.3–3.3 eV), high thermal conductivity, good mechanism strength, and excellent chemical stability.[65] Hao et al.[66] developed a series of SiC nanomaterials with varied morphologies with SF structures, that is, whiskery, particulate, and worm-like. The H_2 production rate of particulate SiC and worm-like SiC stand out as 83.9 and 82.8 μmol h^{-1} g^{-1} in pure water without a sacrificial agent. Furthermore, black phosphorus (BP) was also identified as a good photocatalyst with a visible light response. BP is a layered semiconductor characterized by a narrow band gap that can be adjusted by varying its thickness. The synthesis of BP typically requires high-temperature and high-pressure conditions. In Ozawa et al.'s study, a gentle solvothermal reaction strategy was used to prepare BP nanoparticles, which exhibited rich SF defects and periodic distortion in the *c*-axis direction in the BP crystal. The formation of these SF structures inhibited BP from having a larger sheet-like structure and thus increased the active surface area. The resulting BP with SF exhibited good photocatalytic hydrogen production activity with a 0.48 mmol h^{-1} g^{-1} rate in methanol aqueous solution. However, they observed an activity decrease after the long-term stability test, attributed to the Co–P cocatalyst aggregation and BP morphological alternations. For enhanced photocatalytic stability, it is advisable to use larger sheets of BP with fewer SFs and terminated bonds at the edges of the sheets. **Table** 2 lists different photocatalysts with SF structures for photocatalytic hydrogen production in the literature.

3. SFs-Based Catalysts for OER and Overall Water

3.1. OER

OER occurs at the electrolyzer anode, which is regarded as the bottleneck as it imposes a large intrinsic overpotential (thermal dynamic 1.23 V vs RHE) and sluggish reaction kinetics (4-electron reaction).[68] The development of advanced electrocatalysts with high activity and stability using non-precious metal materials remains a significant challenge.[69] Many researchers found that the introduction of structural defects, in particular, SF defects, can induce a strain effect on the catalyst materials, modifying the electronic structures and electrocatalytic properties.[70] For instance, Pang et al.[71] utilized a hydrothermal method to introduce an abundance of SFs into the Co_3S_4 crystal within Co_3S_4/Ni_3S_2-10%Mo@NC to enhance the OER activity. The Co_3S_4/Ni_3S_2-10%Mo@NC catalyst demonstrated promising OER performance, reaching the current density of 10 and 100 mA cm^{-2} at an overpotential of 164 and 223 mV, respectively, comparable to the OER activity of commercial RuO_2. To analyze strain distribution, they used geometrical phase analysis via Strain++ open-source software, observing tensile and compressive strains and strains distributed along dislocations. It was anticipated that these tensile and compressive strains induced by SFs would influence the charge distribution of Co metal d-orbitals, thereby optimizing the energy associated with the adsorption–desorption of active intermediates on the catalyst surface. In addition to the improved catalytic activity, excellent long-term stability was also demonstrated by the almost unchanged overpotential after the galvanostatic test at 10 mA cm^{-2} for 100 h. By examining the catalyst morphology after the long-term stability test, the structural stability of SFs in the catalyst was investigated in detail. Although the conversion from crystalline to amorphous state after the durability test was demonstrated by SAED and XRD patterns, the lattice distortion didn't change much, and the defects still distributed along the direction of lattice distortion, verifying the good structural stability of SFs in Co_3S_4/Ni_3S_2-10%Mo@NC. In another study centered on $LaNiO_3$ perovskite,[72] researchers leveraged the generation of Ruddlesden–Popper (RP) faults within $LaNiO_3$ epitaxial thin films to induce asymmetry in octahedra, aiming to enhance OER activity. Through precise control of La-excess nonstoichiometry during thin-film deposition, the initial composition was strategically adjusted. This deliberate adjustment introduced RP-type homologous faults, characterized by a consecutive (LaO)–(LaO) stacking pattern, into $LaNiO_3$. The HAADF-STEM results (**Figure** 13a,b) revealed the prevalence of RP-type faults

Table 2. Photocatalytic HER performance for SF defects catalysts.

Catalyst	Preparation method	Medium	H_2 production rate [mmol h^{-1} g^{-1}]	Ref.
Black phosphorus	Solvothermal	20 vol% methanol	0.48	[67]
$Cd_{0.5}Zn_{0.5}S$(en)	Hydrothermal	0.2 м Na_2S and 0.04 м Na_2SO_3	13.54	[63]
$Cd_{0.5}Zn_{0.5}S$(en)NiS	Photodeposition	0.2 м Na_2S and 0.04 м Na_2SO_3	38.19	[63]
NiS/CdS	Hydrothermal	0.5 м Na_2SO_3	49.2	[61]
$Cd_{0.5}Zn_{0.5}S$-CNTs (Cu)	Precipitation-hydrothermal	0.2 м Na_2S and 0.04 м Na_2SO_3	2.99	[64]
CdS nanorods	Precipitation-hydrothermal	0.35 м Na_2S and 0.25 м Na_2SO_3	0.38	[59]
2.0 wt.% Pt/CdS nanorods	Precipitation-hydrothermal	0.35 м Na_2S and 0.25 м Na_2SO_3	5.36	[59]
$Cd0_{.5}Zn_{0.5}S$ nanorod	Hydrothermal microwave	0.35 м Na_2S and 0.25 м Na_2SO_3	2.58	[62]
SiC	Carbothermal reduction	distilled water	0.084	[66]
0.025 wt.% Pt/CdS	Hydrothermal	5 vol% formic acid	0.12	[60]

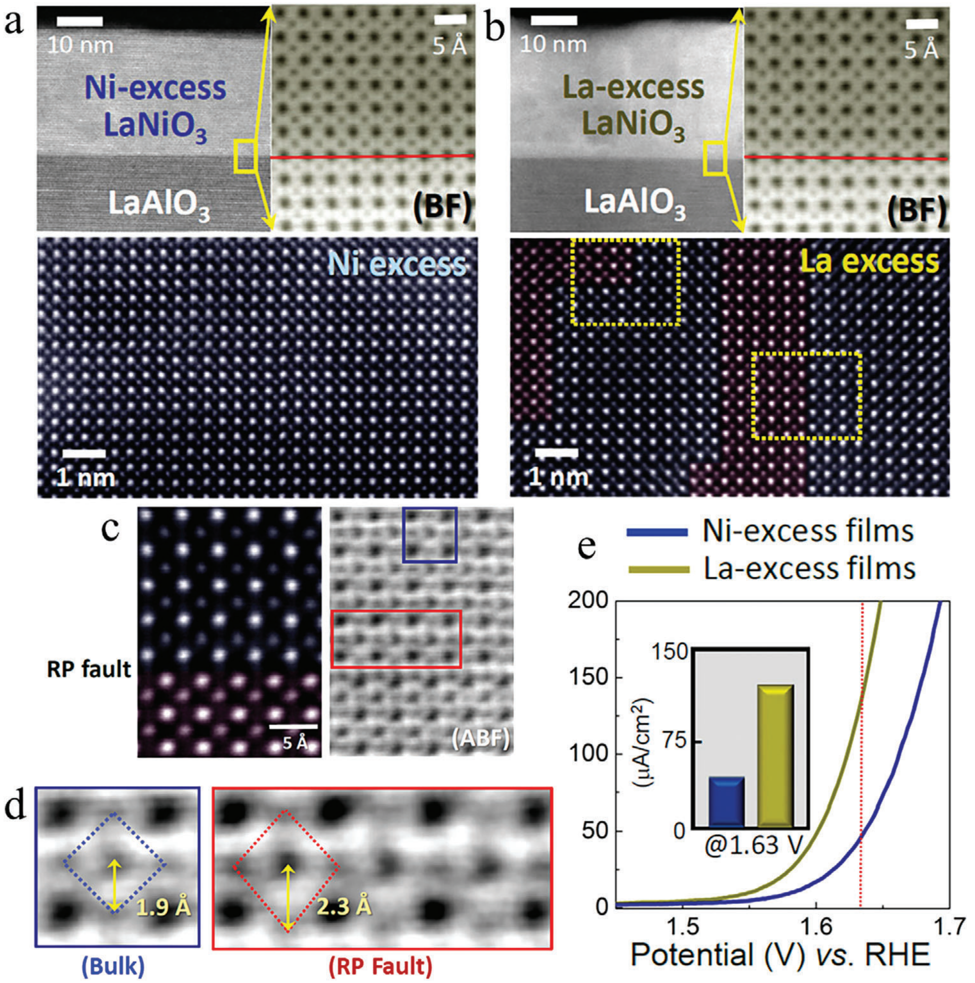

Figure 13. HAADF-STEM and enlarged bright-field (BF) images of a) Ni-excess films, b) La-excess films, c) tetragonal distortion of (NiO_6) octahedra in the RP SFs, and d) bulk (left) and the RP fault region (right), indicating an increase of >20% in the Ni—O bond length, stretching from 1.9 to 2.3 Å. e) Linear sweep voltammetry (LSV) curves for OER over 5%-La-excess and 5%-Ni-excess $LaNiO_3$ catalysts, inset indicates the current densities of two $LaNiO_3$ samples at a potential of 1.63 V versus RHE. Reproduced with permission.[72] Copyright 2017, American Chemical Society.

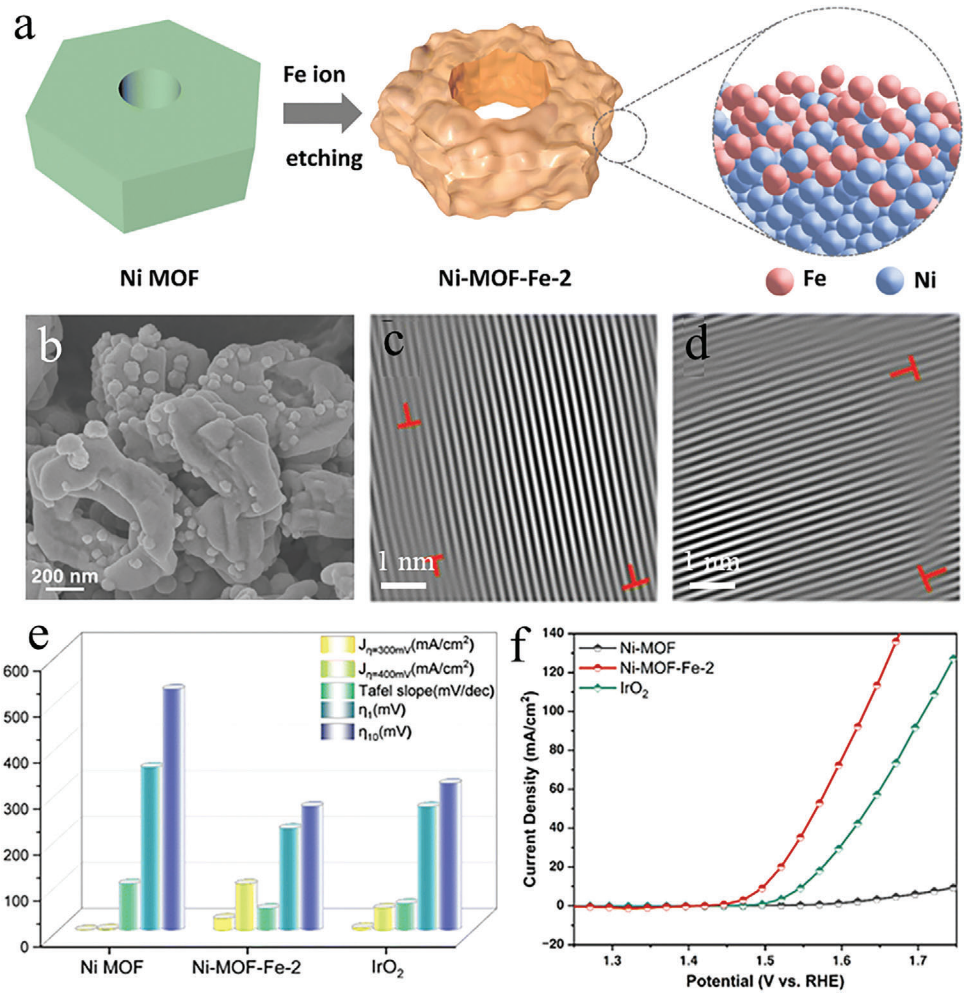

Figure 14. a) Scheme of fabrication of Ni-MOF-Fe-2 catalysts. b) SEM images of Ni-MOF-Fe-2, HRTEM atomic lattice images of c) along the (−121) lattice plane and d) along the (−120) lattice plane. e) The activity results of Ni MOF, Ni-MOF-Fe-2, and IrO$_2$, including the overpotentials (mV) at 1 mA cm^{-2} (η_1) and 10 mA cm^{-2} (η_{10}), the Tafel slopes (mV dec^{-1}), and the current densities (mA cm^{-2}) at 300 mV ($J_{\eta=}$ 300 mV) and 400 mV ($J_{\eta=}$ 400 mV). f) OER LSV curves of Ni MOF, Ni-MOF-Fe-2, and IrO$_2$ without iR-compensation. Reproduced with permission.[73] Copyright 2016, Royal Society of Chemistry.

throughout the 5%-La-excess LaNiO$_3$ films, whereas the 5%-Ni-excess films exhibited minimal lattice fault occurrence. In the fault plane, a significant tetragonal elongation of (NiO$_6$) octahedra was observed due to substantial displacement of apical oxygen, mitigating local repulsive instability stemming from neighboring (LaO)$^+$ layers (Figure 15c,d). The presence of distorted (NiO$_6$) octahedra within the SF emerged as highly active sites for OER, leading to a significantly higher current density in the La-excess thin-film perovskite (Figure 13e). This structural strategy, designed to introduce symmetry-broken octahedra, serves a dual purpose: it lowers the eg level of the metal while elevating the p-band center of oxygen. This approach is anticipated to be pivotal in improving the OER catalysis of perovskites. Additionally, it offers a means to regulate the electron occupancy of the eg-level in perovskite materials.

Mou and co-workers introduced a straightforward method involving the etching of Ni MOF using varying concentrations of Fe ion solution to prepare Ni-MOF-Fe-x materials (**Figure** 14a–d).[73] These MOF materials exhibited enhanced OER performance, showcasing a low overpotential (269 mV at 10 mA cm^{-2}) and a minimal Tafel slope (47.1 mV dec^{-1}), as shown in Figure 14e,f. Incorporating foreign elements resulted in numerous dislocations and SFs forming between the lattice planes within the MOF structure (Figure 14c,d). This arrangement facilitated effective charge transfer, allowing the MOF to abundant active sites. Partial dislocations and SFs in perovskite materials also showed enhanced OER activity.[74] In the research conducted by Zhao and co-workers,[75] they developed a method to produce defect-rich Ni$_3$FeN (DR-Ni$_3$FeN) and nitrogen-doped graphene (N–G) compounds (referred to as DR-Ni$_3$FeN/N-G). The synthetic method involved two steps: temperature-programmed calcination and nitridation treatment of NiFe-LDHs/GO precursors (LDHs: layered double hydroxides; GO: graphene oxide), with precise control over the annealing atmosphere. The resultant catalysts exhibited many defects, including twin crystal defects, grain boundaries, and a noteworthy 10% of SFs. These

Table 3. Electrocatalytic performance of SF-modified catalysts for OER in 1 м KOH unless otherwise specified.

Catalyst	Preparation method	Overpotential @ 10 mA cm^{-2} [mV]	Tafel Slope [mV dec^{-1}]	Stability @ 10 mA cm^{-2} [h]	Ref.
CoCrFeNiMo-20 Mg	Ball milling	220	59	24	[76]
FeCoNiMnCu	Cathodic plasma electrolysis deposition	280	59	40	[77]
$Sr_3NiFeMoO_{9-\delta}$	Sol-gel method	260	42	40 @ 50	[74]
MnFeCoNiCu	Pyrolysis and H_2 thermal treatment	263	43	24	[78]
Double-Shelled NiFe LDH	Self-templated strategy	246 @ 20	71	50 @ 20	[20b]
Ni_3FeN/N-graphene	Temperature-programmed annealing	250	38	12	[75]
Ni_3S_2@Ni–Fe LDH	Hydrothermal synthesis	190	38	40	[79]
Ni-Fe LDHs	Precipitation and template method	280	49	6	[20a]
Au-Ru branched NPs (in 0.1 м $HClO_4$)	Seeded growth	220	62	-	[80]

unique nanohybrids demonstrated remarkable efficiency in catalyzing OER in 1 м KOH, achieving a turnover frequency (TOF) of 0.46 s^{-1} and a minimal overpotential of 250 mV to achieve a current density of 10 mA cm^{-2}. This performance surpassed that of the defect-free Ni_3FeN/N-G and benchmark IrO_2. The study further observed that the abundance of defects in Ni_3FeN NCs enhanced their synergetic interaction with N-G, thereby enhancing the kinetics of interfacial electron transfer in the nanohybrids, ultimately leading to improved OER activity. Apart from their superior activity, these nanohybrids also exhibited enhanced durability in comparison to their counterparts. The robustness of the materials is ascribed to the substantial number of twin boundaries and defects within the Ni_3FeN NCs nanocrystals, effectively dissipating stresses and stabilizing the interface structure. As demonstrated by the microstructural analysis after 2000 cycles, the twin crystal defects (fivefold twinned and microtwinned structures) and grain boundaries in DR-Ni_3FeN NCs can be reserved very well, verifying the good structural stability of these lattice defects during OER conditions. Moreover, the introduction of SF structures in high-entropy alloys such as CoCrFeNiMo-20Mg,[76] FeCoNiMnCu nanoparticles,[77] and MnFeCoNiCu[78] was demonstrated to increase the active surface area, facilitate electron transfer, and enhance the ion conductivity. These enhancements collectively contribute to an advanced electrocatalytic OER performance. The catalytic performance for OER of electrocatalysts featuring SF defects is summarized in **Table 3**.

3.2. Overall Water Splitting

The complete water-splitting process involves the HER at the cathode and the OER at the anode.[81] Developing a bifunctional electrocatalyst that serves as a cathode and anode offers numerous benefits. It simplifies the implementation of the water-splitting system. It helps mitigate significant catalyst degradation and membrane separator issues linked to intermittent operation of renewable energy sources (e.g., solar energy) and redox reactions during water electrolysis.[82] In numerous instances, the improvement in catalytic performance brought about by SF primarily arises from their ability to induce lattice strain, which inherently aids the adsorption–activation–desorption processes during the catalytic reaction. Studies have indicated that subjecting metals to a 1% strain can shift the d-band by ≈0.1 eV, consequently influencing surface adsorbate interactions.[83] Structure defects such as SFs, which perturb the lattice of neighboring atoms, are considered effective strain “carriers”. For instance, Jiang et al.[21] employed a non-equilibrium ultrafast (sub 1s) annealing with the rapid quenching process to fabricate Ru nanoparticles enriched in SF (**Figure 15**a,b). This process resulted in a partial transformation of the closely packed planes, originally exhibiting a perfect hexagonal closed-packed (HCP) with “AB” stacking orders, into a FCC arrangement with an “ABC” configuration situated within the SF region (Figure 15c). These Ru nanoparticles exhibited a remarkably low overpotential of 35 and 196 mV for driving the HER and OER, respectively, at a current density of 10 mA cm^{-2}. This notably expedited the overall water splitting with only 1.51 V in 0.5 м H_2SO_4 (Figure 15d,e). The authors attribute the creation of the SF to a modification in the stacking sequence of the (0002) facet via a 1/3 [1–100] slip. Compressive or tensile strain arises due to the changed atomic spacing of the SF plane and the neighboring facets, which significantly affects Ru’s electronic structure. Moreover, in metals possessing d bands that are more than half-filled, applying tensile strain leads to an upward shift in the d-band center relative to the Fermi level, while using compressive strain results in a downward shift (Figure 15c). In this study, the ordered arrangement of SFs-Ru-NPs induces tension-compression strain pairs, with compressive strain predominantly prevalent. This proves advantageous in fine-tuning the d-band center and mitigating the crystal field splitting effect of active metal sites, facilitating electron transfer and augmenting the OER performance.

Likewise, the introduction of SF defects induced a notable strain effect in an $IrTe_2$ bimetallic alloy.[84] A hollow nanoshuttle-structured IrTe2 enriched with SFs was synthesized using an electrochemical reconstruction approach. Operando XAS results unveiled a reduction in the Ir–O distance from 2.051 to 2.028 Å as the applied potential rose from 0.5 to 1.51 V versus RHE. This observation confirmed the partial oxidation of Ir. This electrochemical dealloying process favored the formation of defects, subsequently leading to an augmentation in the lattice strain of the reconstructed $IrTe_2$. The resultant $IrTe_2$ with abundant SFs demonstrated exceptional performance in the HER with a TOF of 0.71

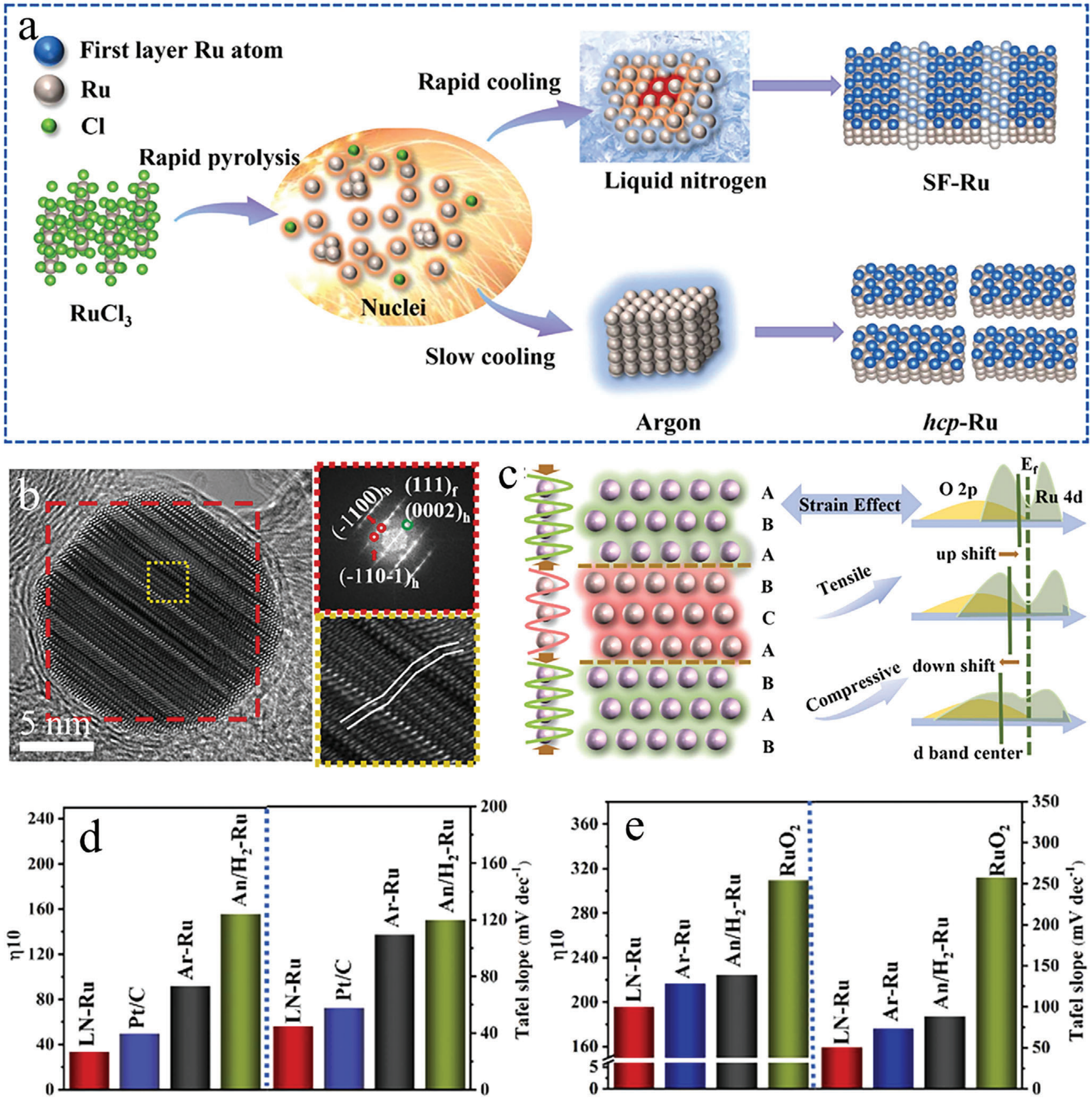

Figure 15. a) Illustration of the synthetic process for SF-rich Ru (SF-Ru) in liquid nitrogen and HCP Ru without SFs in Ar. b) TEM, HRTEM images, and selected area diffraction patterns of SF-Ru. c) Atomic model of SF sequences in HCP-Ru and illustration of the changing of the d-band center along with compressive and tensile strain. d) Overpotential (mV) for HER at 10 mA cm^{-2} (η_{10}) and Tafel slope (mV dec^{-1}) of Ru catalysts and benchmark Pt/C in 1 M KOH. e) Overpotential for OER at 10 mA cm^{-2} (η_{10}) and Tafel slope (mV dec^{-1}) of Ru catalysts and benchmark RuO$_2$ in 0.5 M H$_2$SO$_4$. Reproduced with permission.[21a] Copyright 2022, Elsevier.

H_2 s^{-1} in 1.0 M KOH and OER with a TOF of 0.36 O_2 s^{-1} in 0.5 M H_2SO_4. The integrated D-IrTe$_2$||DO-IrTe$_2$ electrolyzer displayed encouraging performance in the overall water-splitting reaction, achieving current densities of 17.9 and 11.8 mA cm^{-2} at 1.6 V in 1.0 M KOH and 0.5 M H_2SO_4, respectively. Its cell voltage significantly outperformed that of the commercial Pt/C||IrO$_2$ pair. Another noteworthy example of an SFs-induced strain effect was reported by Seidel et al.[55] They achieved heteroepitaxial interphase strain by intentionally introducing SFs and misfit dislocations within porous BaTiO$_3$ nanoparticles. This modification led to an outstanding piezocatalytic performance in water splitting, with the resultant BaTiO$_3$ exhibiting a good hydrogen generation rate of 0.159 mmol g^{-1} h^{-1}. This rate is ≈130 times higher than that of the pristine BaTiO$_3$ catalysts.

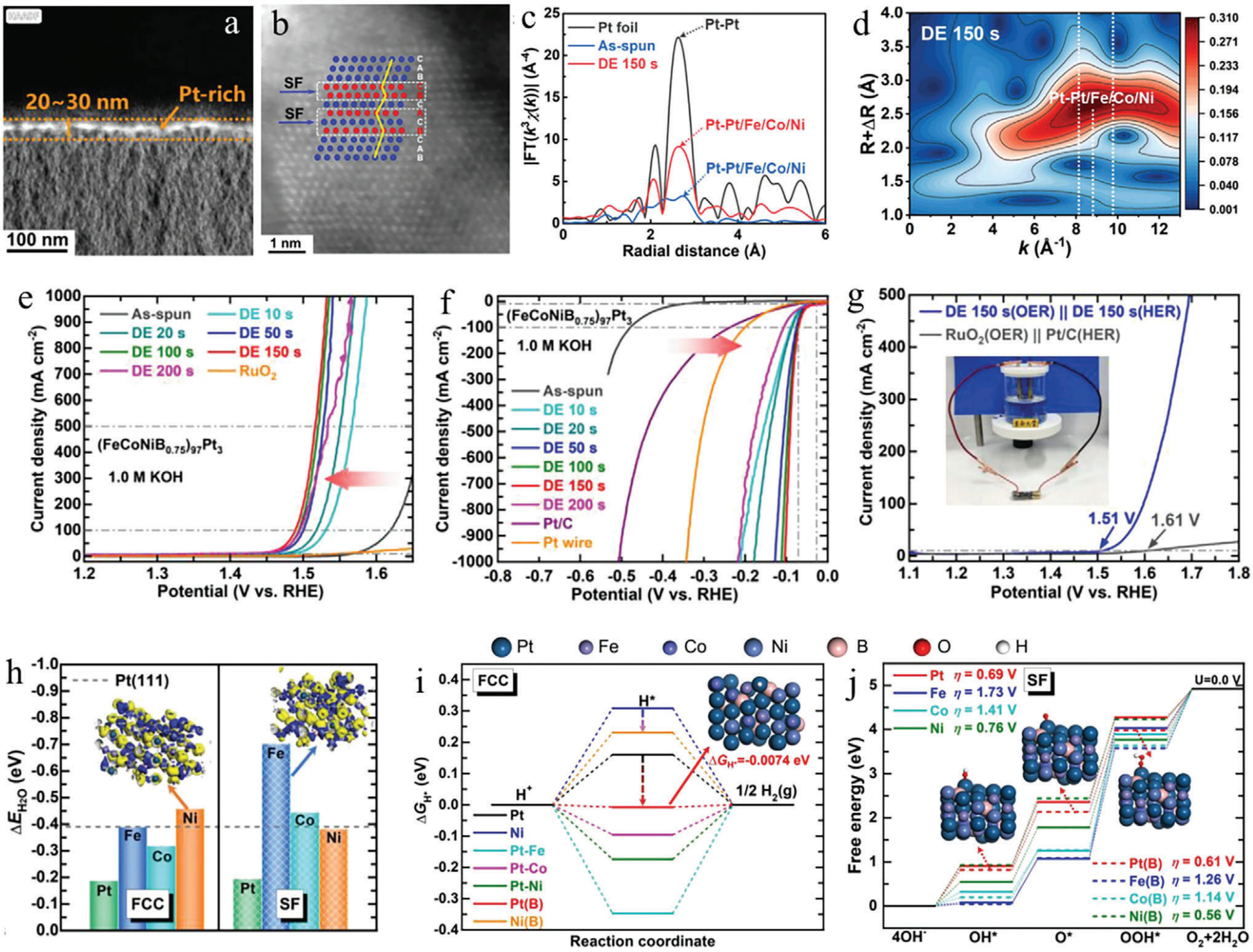

Figure 16. HAADF-STEM image of a) cross-sectional view and b) high resolution of $(FeCoNiB_{0.75})_{97}Pt_3$ HEMG. c) The k3-weighted Fourier transform spectra of the Pt L3-edge. d) Wavelet transform of (c). e) LSV curves for OER and f) LSV curves for HER of HEMG samples, Pt/C, and Pt wire. g) LSV curves for overall water splitting. h) Water molecules absorb energy on different metal sites in FCC and SF structural nanocrystals by DFT calculation. A grey dashed line for reference indicates the energy on the Pt (111) surface. i) ΔG_{H*} profiles on various active sites in the FCC model. The dashed arrows indicate the alternation in ΔG_{H*} after the coordination of B in the active sites. j) Free energy profiles of individual active sites, both with and without B, within the SF structure at potential $U = 0.0$ V. Reproduced with permission.[85] Copyright 2023, Wiley.

Utilizing an electrochemical dealloying strategy, Zhang et al.[85] successfully synthesized a defective nanoporous $(FeCoNiB_{0.75})_{97}Pt_3$ high-entropy metallic glass (HEMG), resulting in the introduction of substantial lattice distortions and SFs within the nanocrystalline structure (refer to the HRTEM images in **Figure** 16a,b and low coordination environment in XAS in Figure 16c,d). This defect-enriched HEMG exhibited remarkable electrocatalytic performance, achieving exceptionally low overpotentials of 104 mV for HER and 301 mV for OER at a high current density of 1000 mA cm^{-2} in 1 м KOH (Figure 16e,f). Additionally, it required a low voltage of 1.65 V to reach the current density of 100 mA cm^{-2} toward overall water splitting (Figure 16g). This performance surpassed currently available catalysts, which often rely on significantly higher quantities of costly noble metals. Noteworthy, the Co and Fe sites within the SF structure possessed the largest water adsorption energies, surpassing that of Pt (Figure 16h). The addition of B induced alterations in the coordination environments, generating abundant SF structures. This, in turn, demonstrated a favorable adsorption capacity for H* and enhanced electron transferability (Figure 16i,j), both crucial factors contributing significantly to the enhanced activity for water splitting. The metal carbide family has also attracted extensive attention as potential electrocatalysts for overall water splitting, given its low overpotential, good conductivity, and durability. Nguyen and co-workers[86] have developed a scalable route to synthesize M_xCs (M = Ni, Co, and Fe), and a large density of SF was induced into the M_xCs carbides via transformation of Prussian blue precursors through solvothermal processing, of which Ni_3C exhibited good catalytic performance as bifunctional HER and OER electrocatalyst for water electrolysis (412 and 503 mV overpotential at 10 mA cm^{-2} for HER and OER, respectively). In the study conducted by Ye and co-workers,[87] a Ni-Fe LDHs electrocatalyst featuring dislocations and SFs was synthesized, resulting in a considerable

Table 4. Electrocatalytic performance of SF-modified catalysts for OER, HER, and overall water splitting in 1 M KOH unless otherwise specified.

Catalyst	OER		HER		Medium	Overall Water Splitting	Stability	Ref.
	Overpotential @ 10 mA cm^{-2} [mV]	Tafel Slope [mV dec^{-1}]	Overpotential @ 10 mA cm^{-2} [mV]	Tafel Slope [mV dec^{-1}]		Potential @ 10 mA cm^{-2} [V]	@ mA cm^{-2}	
$(FeCoNiB_{0.75})_{97}Pt_3$	170	38	27	31	1.0 M KOH	1.51	200 h @ 100 mA cm^{-2}	[85]
$Co_{0.03}$-$NiFe_{0.97}$ LDH	280@50	94	170	97	1.0 M KOH	1.53 @ 50	10 h@10	[87]
NiTe-NiSe	164	53	76	62	1.0 M KOH	1.49	100 h@100	[88]
Co_2C-PBA (Prussian blue analog)	423	145	566	-	1.0 M KOH	-	-	[86]
Fe_3C-PBA	576	165	800	-	1.0 M KOH	-	-	[86]
Ni_3C-PBA	503	112	412	170	1.0 M KOH	-	-	[86]
SF-Ru NPs	196	51	35	45	HER: 1.0 M KOH OER: 0.5 M H_2SO_4	1.51	24	[21a]
$IrTe_2$ hollow nanoshuttles	250	49	54	33	HER: 1.0 M KOH OER: 0.5 M H_2SO_4	1.6	-	[84]
Co_2P/Ni_2P-2%Mo	319@50	46	118@50	45	1.0 M KOH	1.57	50@60	[17a]
Ni_2P	350	65	240	80	1.0 M KOH	1.80	7@35	[89]
Ni_5P_4	-	-	190	70	1.0 M KOH	-	-	[89]
3D iron fluoride-oxide nanoporous film	260	45	20	31	1.0 M KOH	1.58	8	[21b]

enhancement in water splitting performance. It displayed a commendable overpotential of 280 mV for catalyzing the OER at 50 mA cm^{-2} and 170 mV for the HER at a current density of 10 mA cm^{-2}. Furthermore, achieving a current density of 50 mA cm^{-2} for overall water splitting necessitated a low voltage of 1.53 V. The catalytic activity for OER, HER, and water splitting of electrocatalysts featuring SF defects are summarized in **Table** 4.

4. SFs-Based Catalysts for Other Electrocatalytic Applications

SF defect engineering is also applied to design catalysts to improve various other electrocatalytic reactions, such as electrocatalytic oxidation reactions. Ramadhan et al.[40] precisely controlled the formation of SFs in 3D branched Ni nanoparticles by adjusting the quantity of HCP-FCC crystal phase transitions (**Figure** 17). The modulation of the width of the Ni branch enabled the formation of distinct proportions of FCC and HCP Ni crystal phases. During each transition between these two crystal segments, there was a disruption in the stacking order, leading to the creation of SFs. The augmentation in SF density, rising from 5% to 11%, translated to a notable 3.5 times improvement in performance toward 5-hydroxymethylfurfural (HMF) oxidation (Figure 17f–h). In Figure 17i,j, the oxidation peak of Ni^{2+} to Ni^{3+} was observed at ≈1.43 V RHE for the Ni with 11% fault density. This peak potential was 38 mV lower than Ni's, with a 5% fault rate. This discrepancy bears significance, as a 38 mV reduction in potential corresponds to a roughly fivefold increase in the production of Ni^{3+} according to the Nernst equation. The formation of a greater number of Ni^{3+} at lower potentials holds relevance for catalytic reactions necessitating Ni^{3+} participation, for example, the electrocatalytic oxidation of HMF. DFT calculations demonstrated the impact of SFs on the creation of active Ni^{3+} species. The analysis showed that the energy alternation for Ni—OH to Ni—O oxidation was reduced at the Ni SF (0.20 eV) in comparison to the pristine Ni($10\bar{1}0$) (0.31 eV). The greater favorability in energy change suggested that atoms at SF sites underwent oxidation more readily, resulting in the generation of active Ni^{3+} sites, thereby facilitating the HMF oxidation reaction. In another study by Cui et al.,[90] the defect-rich AuPtNi alloy nanostructures were synthesized and exhibited good ethanol oxidation reaction (EOR) and methanol oxidation reaction (MOR) activity in acid. The presence of defects, including SFs, twins, and atomic steps in AuPtNi, granted significant access to active sites for the oxidation reaction, resulting in an electrochemically active surface area of ≈51 m^2 g^{-1}, which closely approached that of commercial Pt/C (54 m^2 g^{-1}). The mass activity of the defective AuPtNi NSs toward MOR and EOR were 996 and 794 mA $mg_{Pt}{}^{-1}$, which were ≈3.1- and 2.4-folder higher than that of the commercial Pt/C catalyst (318 and 336 mA $mg_{Pt}{}^{-1}$). In another study, through a facile chemical reduction method, Lu and co-workers[47] successfully created high-density SFs (HDSFs) into ultrathin Au nanowires to obtain ultrathin AuNWs, which was used as an efficient electrocatalyst for MOR. In both acid and alkaline media, the resulting AuNWs with HDSF structure exhibited much better MOR activity than the poly-Au nanoparticles and bulk Au. This enhancement can be attributed to their improved adsorption capacity for $OH^-{}_{ads}$, which arises from the presence of SFs in their structures.

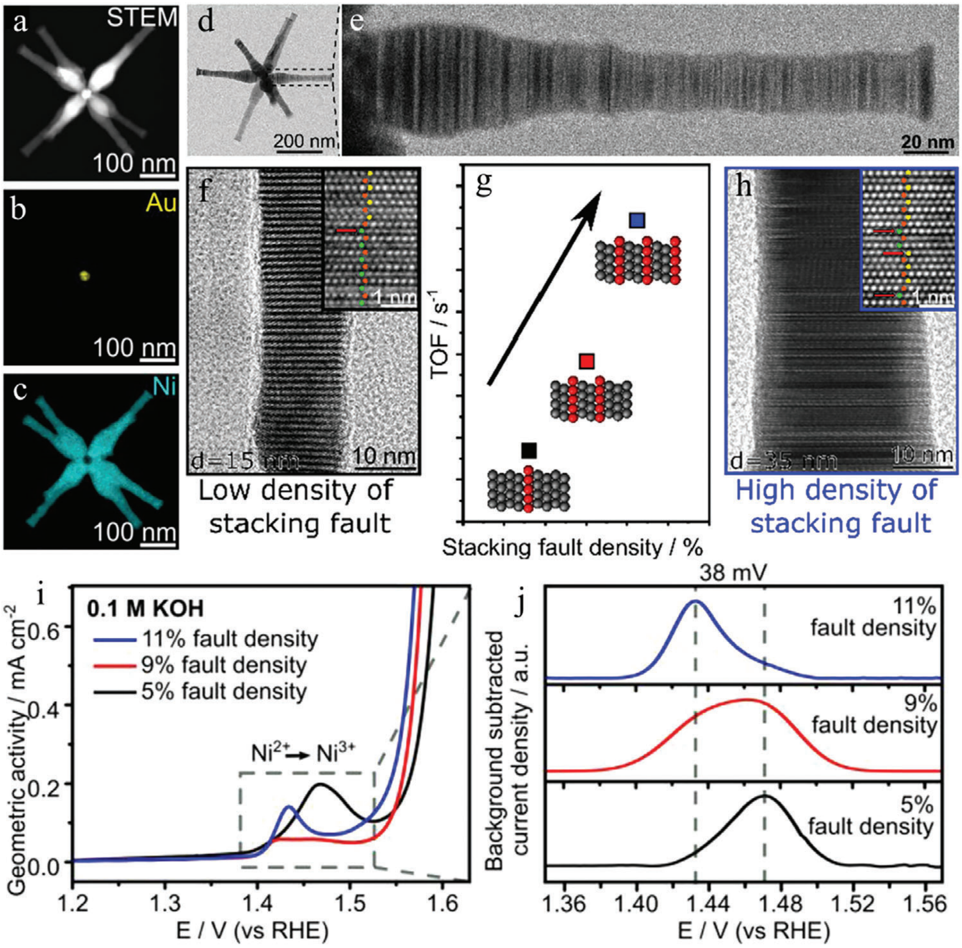

Figure 17. a) HAADF-STEM image of one branched nanoparticle. b) EDX mapping image of Au. c) EDX mapping image of Ni. d) TEM of Ni branched nanoparticle. e) HRTEM images of a Ni branch. f) HRTEM image of a Ni branch 15 nm in width with low density of SF. g) TOF values of Ni catalysts with varied SF densities. h) HRTEM image of a Ni branch 34 nm in width with a high density of SF. i) LSV curves for OER of Ni catalysts with varied SF rates in 0.1 M KOH. j) Plots of background subtracted current densities against the potential range where the oxidation of Ni^{2+} to Ni^{3+} occurred. Reproduced with permission.[40] Copyright 2022, American Chemical Society.

SFs-incorporated catalysts were also developed for improved electrocatalytic reduction reactions, such as ORR,[22,43,91] CO_2RR,[92] and NO_3RR.[51] Precious metals such as Pd, Pt, Ir, Au, Ru, and Ag are promising electrocatalysts for ORR. The incorporation of SF into metal catalysts has been reported to improve the ORR activity and stability significantly. For example, Ag nanoparticles with abundant surface SF defects created via laser ablation in liquid strategy showed much better ORR activity (onset potential of 980 mV, Tafel slope of 74 mV dec^{-1}) than their Ag counterpart (onset potential of ≈800 mV, Tafel slope of 97 mV dec^{-1}) without defects and Pt/C (onset potential of ≈983 mV, Tafel slope of 85 mV dec^{-1}) (**Figure** 18a–c).[22] Wang et al.[22] developed an ultralong Ag nanowires catalyst and observed a 20% increase in the diffusion-limiting current density of ORR, which increased from 4.98 to 6.00 mA cm^{-2} following sonication straining (Figure 18d–f) and the significant ORR activity improvement is due to the generation of many kinds of defects such as twin crystals, dislocations, and SF that elevate the surface energy and attenuate the binding between the adsorbates and Ag surface. Kudo et al.[93] used arc-plasma deposition method to deposit Pt and Zr on Pt(111) surface to fabricate Pt/Zr/Pt(111) electrocatalyst, which demonstrated three to five times greater ORR activities compared to the pristine Pt(111) surface (Figure 18g–i). They observed the formation of SF in the underlying Pt–Zr alloy layers, which triggered tensile strains in the Pt-shell. The ORR current densities plotted against strain demonstrated a volcano-shaped curve, with the highest current density at ≈2% compressive strain on the surface (Figure 18j). The author proposed two effects that may influence the ORR activity significantly. The surfaces of the Pt-shell could potentially undergo electronic modifications due to charge transfers occurring between Zr and Pt, often referred to as the ligand effect. Furthermore, the compressive strains the Pt-shells experienced reduced the adsorption energy of oxygen-related species, usually referred to as the strain effect. Additionally, PtAgPb core–shell nanoplates with SF induced by oxidative etching were shown excellent ORR activity.[43] They displayed superior specific activity at 5.06 mA cm^{-2} and mass activity at 2.24 A mg_{Pt}^{-1} for ORR, respectively 18 and 13 times greater than those of Pt/C. They used theoretical calculation to reveal that the downward shift of the d-band center of Pt atoms

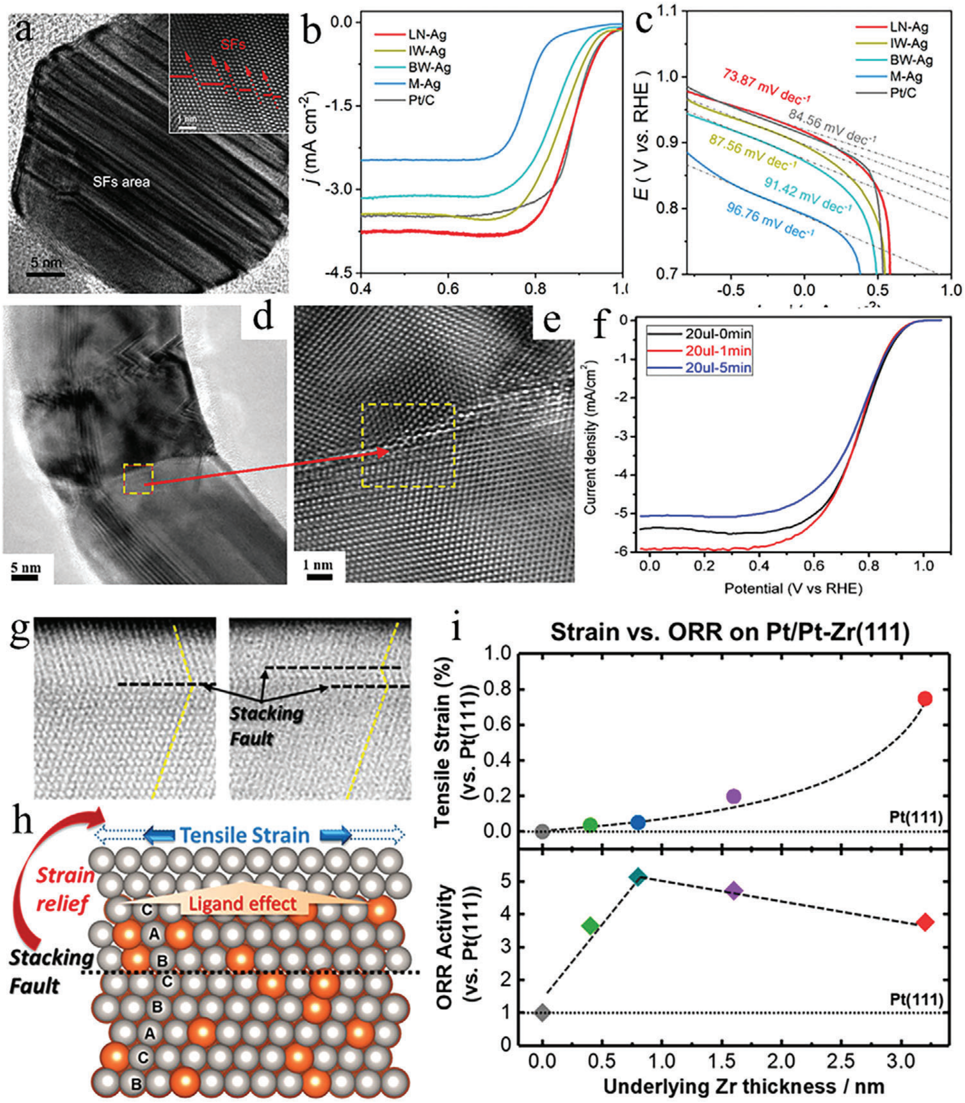

Figure 18. a) TEM and HRTEM (insert) images of Ag nanoparticles with SFs. b) ORR LSV curves and c) Tafel plots of Ag nanoparticles and Pt/C in O_2-saturated 1 M KOH (LN-Ag: liquid nitrogen (high density of SFs), IW-Ag: ice water (moderate density of SFs), BW-Ag: boil water (low density of SFs), M-Ag: monocrystal Ag (no SFs)). Reproduced with permission.[22a] Copyright 2023, American Chemical Society. d) TEM image and e) HRTEM image of deformed Ag nanowires. f) ORR LSV curves of Ag nanowires with 0-, 1-, and 5-min sonication times in O_2-saturated 0.1 M KOH. Reproduced with permission.[22b] Copyright 2021, American Chemical Society. g) STEM image of Pt/Zr/Pt(111). h) atomic model of SF and tensile strain in Pt. i) Plots of tensile strains (top) and ORR activity (bottom) in relation to the deposition thickness of the third layer Zr (which forms the underlying Pt-shell). Reproduced with permission.[93] Copyright 2019, American Chemical Society.

caused by SF proved beneficial in effectively removing oxygen-containing species from the surfaces, owing to their decreased adsorption strength. This consequently led to a substantial increase in ORR activity for the SF-featured PtAgPb catalyst. Another Pt-based catalyst PtNi alloy with dense structural defects (SFs) exhibited 9.3 times improvement of the ORR-specific activity compared to Pt/C,[91] further endorsing the promotive effect of SF defects on ORR activity. Furthermore, by transforming pristine Cu oxides into Cu through alkaline solution treatment, Fang et al.[51] fabricated the oxide-derived Cu with a high SF defects rate on Cu foam, showing significant improvement toward the NO_3RR process. The SF on Cu caused tensile strain, a condition favorable for nitrate adsorption. This also increased the number of intrinsically active sites for the reduction reaction. In addition, the SFs-modified materials were also reported for electrochemical applications such as Li_2RuO_3[35] and LixMnO_3[24] for Li-ion batteries, NiMo-LDH for supercapacitor electrodes,[24] Y_2Ni_7 for hydrogen storage.[94] The catalytic activity for various applications by electrocatalysts featuring SF defects is summarized in **Table 5**.

5. Conclusion

This review has explored the critical role of SF defects in catalyst materials, with a particular focus on their potential to enhance hydrogen generation through various electrocatalytic processes. The intentional introduction of SF hs emerged as a promising

Table 5. Electrocatalysts featuring SF defects for various electrocatalytic reactions.

Catalyst	Preparation method	Applications	Performance	Ref.
Ag nanoparticles	Laser ablation in liquid	Zn-air batteries	Power density: 262.85 mW cm^{-2}	[22a]
PtAgPb-IV/C nanoplates	Oxidative etching	ORR	Mass activities: 2.24 A mg_{Pt}^{-1} Onset potential: 1.05 V vs RHE Limiting current density: 5.8 mA cm^{-2}	[43c]
Ag nanowires	Sonication	ORR	Onset potential: 0.95 V vs RHE Limiting current density: 5.91 mA cm^{-2}	[22b]
Pd nanoparticles	Laser ablation in liquid	ORR	Onset potential: 0.82 V vs RHE Limiting current density: 6.0 mA cm^{-2}	[95]
PtNi/C	Polyol synthesis	ORR	Mass activities: 852 ± 219 μA mg_{Pt}^{-1}	[91]
Pt/Zr/Pt(111)	APD deposition	ORR	5 times higher than Pt(111)	[93]
Pt/Y:TiO_2-C	photo-deposition	ORR	Mass activities: 40 mA mg_{Pt}^{-1}	[22c]
Oxide-derived Cu/Cu foam	Alkaline oxidation	NO_3RR	Great nitrate-N removal: 93% Ammonia-N selectivity: 94% Ammonia Faradaic efficiency: 80%	[51]
NiMn-LDH	Hydrothermal	Supercapacitor	Capacity:1498 C g^{-1} at 2 A g^{-1}	[24c]
AuPtNi	Solvothermal	MOR and EOR	Mass activities of MOR: 996.3 mA mg_{Pt}^{-1}, EOR: 794.0 mA mg_{Pt}^{-1}	[90]
Au nanowires	Solvent reduction	MOR	140 μA cm^{-2} at 0.8 V vs Hg/HgO	[47]
Li_2MnO_3	Annealing	Li-ion battery cathode	N/A	[24b]
Li_2MnO_3	Annealing	Li-ion battery cathode	N/A	[24a]
Li_xMnO_3	Annealing	Li-ion battery cathode	N/A	[24d]
Li_2RuO_3	Annealing	Li-ion battery cathode	N/A	[35]
Y_2Ni_7	Annealing and quenching	H_2 storage	H_2 storage capacity: Good	[94]
Sm_2Ni_7	Annealing and quenching	H_2 storage	H_2 storage capacity: Bad	[94]
Gd_2Ni_7	Annealing and quenching	H_2 storage	H_2 storage capacity: Moderate	[94]
$La_{0.8}Mg_{0.2}Ni_{3.67}$	Annealing and quenching	H_2 storage	H_2 storage capacity: Good	[94]

avenue, showcasing the potential to alter the properties of catalysts, influence surface reactivity, and create additional active sites. These transformative effects result in significant improvement in catalytic activity and stability. The thorough investigation of SF has unveiled their potential applications in a wide range of electrocatalytic reactions, ranging from oxygen evolution and reduction to (photo-/electrocatalytic) hydrogen evolution and other processes like nitrate and carbon dioxide reduction (**Scheme 1**). The presence of SF defects in electrocatalysis holds great potential, yet several significant questions remain unanswered. To propel this field forward, we identify specific areas worthy of future research:

- Innovative Synthesis Techniques: To synthesize catalysts rich in SF defects, precision is paramount. Achieving a specific density and uniform distribution of SFs across various nanomaterials demands sophisticated techniques and a deep understanding of the material's crystal structure. Essential to this endeavor is the implementation of advanced synthesis methods, enabling precise control over defect formation. Moreover, the design and synthesis of hierarchical nanostructures, incorporating SF defects at different levels (e.g., core–shell, heterostructure, and hybrid structures), emerge as pivotal strategies. This approach aims not only for the introduction of SF defects but also for the creation of multifunctional and synergistic electrocatalytic platforms. The investigation and modulation of the interaction between SF defects and other factors, such as doping, strain, surface area, and morphology, become imperative. This meticulous exploration seeks to fine-tune and enhance the catalytic properties of the catalyst materials.
- Advanced Characterization Techniques: Accurate characterization techniques are required to assess these defects' density and distribution. Currently, commonly employed methods, such as electron microscopy (e.g., HRTEM) and X-ray techniques (e.g., XRD), have been instrumental in assessing the density and distribution of SFs. However, as the field progresses, there is a compelling need to explore and implement cutting-edge characterization technologies to unlock more detailed insights into the properties of SF. The evolution of characterization tools promises a leap forward in understanding the intricate details of SF defects. Emerging techniques may encompass advancements in electron microscopy, such as advanced TEM and STEM. Additionally, synchrotron-based X-ray methods (e.g., XAS) could offer enhanced capabilities for probing the electronic structure of SF with unprecedented precision. Moreover, the integration of spectroscopic

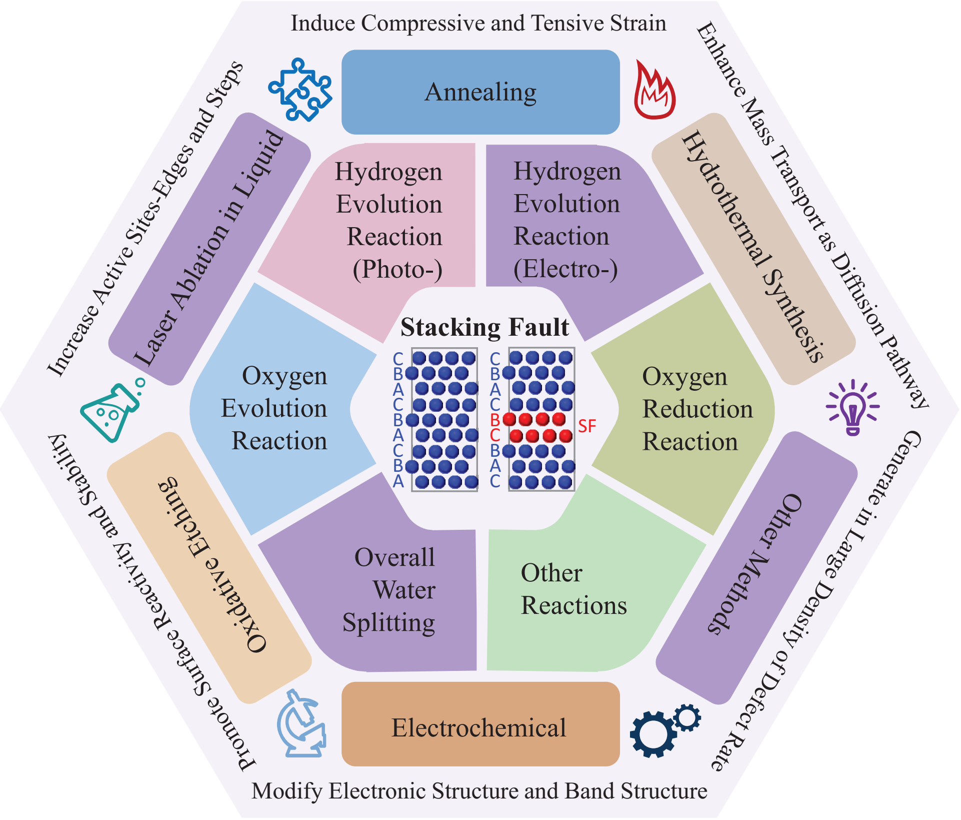

Scheme 1. Overview of review scope on SF-based catalysts.

techniques, such as Raman spectroscopy and vibrational spectroscopy, holds the potential for providing additional layers of information regarding the vibrational and chemical characteristics of SF. Developing and applying cutting-edge characterization technologies will provide crucial knowledge of the nature of SF, allowing for more accurate assessments of their impact on catalyst performance.

- Operando Studies for Real-Time Insight: Future investigations may prioritize operando studies, allowing real-time monitoring of SF-induced changes during catalytic reactions. This approach could unveil dynamic aspects of SF behavior under working conditions, offering insights into the evolution of defects during various stages of electrocatalysis. The integration of advanced in situ techniques, such as operando XRD and operando spectroscopies, emerges as a powerful toolset for comprehensive exploration. Operando XRD allows for the real-time observation of structural changes within the catalyst during electrocatalytic processes, offering valuable information on phase transitions, lattice distortions, and the redistribution of SFs. Concurrently, operando spectroscopy techniques, including infrared and Raman spectroscopy, contribute to elucidating the chemical transformations occurring at the catalyst surface during dynamic electrochemical reactions. By harnessing operando studies, researchers gain access to a wealth of information on the transient states of catalysts in action. This not only refines our understanding of how SF defects evolve during catalytic reactions but also provides critical insights for designing more robust materials. The ability to observe and comprehend these transient states in real time facilitates the optimization of catalyst structures, ensuring their efficacy and stability under practical operating conditions.
- Understanding the Influence on Catalytic Activity: A comprehensive understanding of how SF defects influence catalytic activity is yet to be systematically investigated and clearly defined. A profound understanding of the intricate relationship between SF properties and catalytic behavior is essential for harnessing their full potential. This requires advanced computational modeling, in-depth spectroscopic analyses, and experimental studies under operando conditions. Such endeavors will pave the way for the design and optimization of catalysts with tailored defect structures to achieve even greater efficiencies in hydrogen generation and other electrocatalytic applications.
- Integration of Machine Learning in Catalyst Design: Harnessing the power of machine learning algorithms presents an exciting avenue. Future research could explore the integration of machine learning techniques to predict optimal defect configurations for targeted catalytic reactions. By leveraging data from diverse sources, including experimental results and theoretical calculations, machine learning models could guide researchers toward designing catalysts with tailored defect structures, streamlining the materials discovery process.
- Tailored Defect Structures for Specific Applications: Tailoring defect structures in catalysts to suit specific electrocatalytic applications is a compelling avenue for advanced material development. This approach involves tailoring the structural defects

of the catalyst to meet the unique requirements of the catalytic reaction, thereby optimizing the performance of the target reaction. Potential strategies for exploring this tailoring process involve a careful balance between defect type, density, distribution, and the specific requirements of the desired application. This nuanced design approach promises superior catalytic activity and stability, contributing to the broader goal of developing efficient, multifunctional catalysts for sustainable energy technologies.

- Environmental Impact Assessment of Catalysts: As sustainable practices gain prominence, future research could incorporate an environmental impact assessment of catalysts enriched with SF defects. This could involve evaluating the life cycle analysis, resource efficiency, and recyclability of such catalysts. Understanding the broader environmental implications of SF-modified catalysts will contribute to the development of green and sustainable electrocatalytic technologies.

In conclusion, exploiting SF defects in catalyst materials represents a promising avenue for advancing sustainable enegy technologies. Through concerted research efforts and interdisciplinary collaborations, we are poised to unlock the full potential of SF as catalyst modifiers, ushering in a new era of efficient and environmentally friendly hydrogen generation.

Acknowledgements

This study was financially supported by the Alfred Deakin Research Fellowship and the International Hydrogen Research Fellowship Program. Y.W. acknowledges the financial support from CSIRO, the Department of Climate Change, Energy, the Environment and Water (DCCEEW) Australian Government, and the Australian Hydrogen Research Network (AHRN). The authors acknowledge the Australian Research Council (DE230100327 and LP220200583). H.A. and Y.S. acknowledge the support from the DCCEEW International Clean Innovation Researcher Networks Grant (ICIRN000011).

Open access publishing facilitated by The University of Melbourne, as part of the Wiley - The University of Melbourne agreement via the Council of Australian University Librarians.

Conflict of Interest

The authors declare no conflict of interest.

Keywords

catalysts, defect engineering, electrocatalytic reactions, hydrogen production, stacking faults (SFs)

Received: December 8, 2023
Revised: February 2, 2024
Published online: March 5, 2024

---

[1] a) T. N. Veziroğlu, S. Şahi˙n, *Energy Convers. Manage.* **2008**, *49*, 1820; b) J. O. Abe, A. P. I. Popoola, E. Ajenifuja, O. M. Popoola, *Int. J. Hydrogen Energy* **2019**, *44*, 15072; c) A. Midilli, M. Ay, I. Dincer, M. A. Rosen, *Renewable Sustainable Energy Rev.* **2005**, *9*, 255.

[2] a) M. K. Singla, P. Nijhawan, A. S. Oberoi, *Environ. Sci. Pollut. Res.* **2021**, *28*, 15607; b) Y. Haseli, *Int. J. Hydrogen Energy* **2018**, *43*, 9015; c) D. D. T. Ferraren-De Cagalitan, M. L. S. Abundo, *Renewable Sustainable Energy Rev.* **2021**, *151*, 111413.

[3] Y. Manoharan, S. E. Hosseini, B. Butler, H. Alzhahrani, B. T. F. Senior, T. Ashuri, J. Krohn, *Appl. Sci.* **2019**, *9*, 2296.

[4] a) J. Chi, H. Yu, *Chin. J. Catal.* **2018**, *39*, 390; b) D. L. Stojić, M. P. Marčeta, S. P. Sovilj, Š. S. Miljanić, *J. Power Sources* **2003**, *118*, 315; c) M. Wang, Z. Wang, X. Gong, Z. Guo, *Renewable Sustainable Energy Rev.* **2014**, *29*, 573.

[5] a) Y. Zheng, Y. Jiao, A. Vasileff, S. Z. Qiao, *Angew. Chem., Int. Ed.* **2018**, *57*, 7568; b) F. Safizadeh, E. Ghali, G. Houlachi, *Int. J. Hydrogen Energy* **2015**, *40*, 256; c) J. Wei, M. Zhou, A. Long, Y. Xue, H. Liao, C. Wei, Z. J. Xu, *Nano-Micro Lett.* **2018**, *10*, 75.

[6] a) T. Reier, H. N. Nong, D. Teschner, R. Schlögl, P. Strasser, *Adv. Energy Mater.* **2017**, *7*, 1601275; b) L. Li, P. Wang, Q. Shao, X. Huang, *Adv. Mater.* **2021**, *33*, 243; c) Z. Shi, X. Wang, J. Ge, C. Liu, W. Xing, *Nanoscale* **2020**, *12*, 13249.

[7] a) X. Xie, L. Du, L. Yan, S. Park, Y. Qiu, J. Sokolowski, W. Wang, Y. Shao, *Adv. Funct. Mater.* **2022**, *32*, 2110036; b) F. Song, L. Bai, A. Moysiadou, S. Lee, C. Hu, L. Liardet, X. Hu, *J. Am. Chem. Soc.* **2018**, *140*, 7748.

[8] a) J. S. Yoo, X. Rong, Y. Liu, A. M. Kolpak, *ACS Catal.* **2018**, *8*, 4628; b) A. Zagalskaya, V. Alexandrov, *ACS Catal.* **2020**, *10*, 3650; c) Y. Zhu, H. A. Tahini, Z. Hu, Y. Yin, Q. Lin, H. Sun, Y. Zhong, Y. Chen, F. Zhang, H. J. Lin, C. T. Chen, W. Zhou, X. Zhang, S. C. Smith, Z. Shao, H. Wang, *EcoMat* **2020**, *2*, e12021.

[9] a) Y. Yin, A. P. Alivisatos, *Nature* **2005**, *437*, 664; b) C. Wang, Q. Zhang, B. Yan, B. You, J. Zheng, L. Feng, C. Zhang, S. Jiang, W. Chen, S. He, *Nano-Micro Lett.* **2023**, *15*, 52.

[10] a) Y. Du, B. Li, G. Xu, L. Wang, *InfoMat* **2023**, *5*, e12377; b) V. R. Stamenkovic, D. Strmcnik, P. P. Lopes, N. M. Markovic, *Nat. Mater.* **2017**, *16*, 57.

[11] M. Luo, S. Guo, *Nat. Rev. Mater.* **2017**, *2*, 17059.

[12] a) D. Yan, C. Xia, W. Zhang, Q. Hu, C. He, B. Y. Xia, S. Wang, *Adv. Energy Mater.* **2022**, *12*, 2202317; b) X. Yan, L. Zhuang, Z. Zhu, X. Yao, *Nanoscale* **2021**, *13*, 3327; c) T. Tang, Z. Wang, J. Guan, *Chin. J. Catal.* **2022**, *43*, 636.

[13] Y. Zhang, H. Liu, S. Zhao, C. Xie, Z. Huang, S. Wang, *Adv. Mater.* **2023**, *35*, 2209680.

[14] L. Fang, S. Lu, S. Wang, X. Yang, C. Song, F. Yin, H. Liu, *Chem. Eur. J.* **2024**, 202303249.

[15] H. Arandiyan, S. S. Mofarah, C. C. Sorrell, E. Doustkhah, B. Sajjadi, D. Hao, Y. Wang, H. Sun, B.-J. Ni, M. Rezaei, Z. Shao, T. Maschmeyer, *Chem. Soc. Rev.* **2021**, *50*, 10116.

[16] A. Mahmood, H. Lin, N. Xie, X. Wang, *Chem. Mater.* **2017**, *29*, 6329.

[17] a) H. Liu, M. Jin, D. Zhan, J. Wang, X. Cai, Y. Qiu, L. Lai, *Appl. Catal., B* **2020**, *272*, 118951.

[18] X. Wang, Y. Ge, Q. Zhang, T. Lin, B. Chen, L. Li, Z. Huang, Q. Yun, X. Zhou, Z. Shi, G. Liu, J. Liu, G. Wang, L. Zheng, B. Huang, L. Liao, Y. Yao, L. Zhai, S. Lu, Q. Luo, Y. Chen, L. Gu, H. Zhang, *Nat. Sci.* **2022**, *2*, 20220026.

[19] Z. Li, J.-Y. Fu, Y. Feng, C.-K. Dong, H. Liu, X.-W. Du, *Nat. Catal.* **2019**, *2*, 1107.

[20] a) L. Yu, J. F. Yang, B. Y. Guan, Y. Lu, X. W. Lou, *Angew. Chem., Int. Ed.* **2018**, *57*, 172; b) J. Zhang, L. Yu, Y. Chen, X. F. Lu, S. Gao, X. W. Lou, *Adv. Mater.* **2020**, *32*, 1906432.

[21] a) R. Jiang, Y. Da, J. Zhang, H. Wu, B. Fan, J. Li, J. Wang, Y. Deng, X. Han, W. Hu, *Appl. Catal., B* **2022**, *316*, 121682; b) X. Fan, Y. Liu, S. Chen, J. Shi, J. Wang, A. Fan, W. Zan, S. Li, W. A. Goddard, X.-M. Zhang, *Nat. Commun.* **2018**, *9*, 1809.

[22] a) W.-J. Kang, Y. Feng, Z. Li, Z.-N. Chen, C.-K. Dong, J. Yang, P.-F. Yin, H. Liu, X.-W. Du, *ACS Energy Lett.* **2023**, *8*, 3512; b) Z. Wang, X. Cao, D. Peng, Y. Lu, B. Zhang, K. Huang, T. Zhang, J. Wu, Y. Huang, *J.*

Phys. Chem. Lett. **2021**, *12*, 2029; c) L. A. Estudillo-Wong, Y. Luo, J. A. Díaz-Real, N. Alonso-Vante, *Appl. Catal., B* **2016**, *187*, 291.

[23] L. Fang, S. Lu, H. Liu, presented at *ECS. Meeting Abstracts*, Vancouver-Canada, May **2022**.

[24] a) X. Li, X. Li, L. Monluc, B. Chen, M. Tang, P.-H. Chien, X. Feng, I. Hung, Z. Gan, A. Urban, Y.-Y. Hu, *Adv. Energy Mater.* **2022**, *12*, 2200427; b) B. Wang, Z. Zhuo, H. Li, S. Liu, S. Zhao, X. Zhang, J. Liu, D. Xiao, W. Yang, H. Yu, *Adv. Mater.* **2023**, *35*, 2207904; c) Z. Zhang, H. Huo, L. Wang, S. Lou, L. Xiang, B. Xie, Q. Wang, C. Du, J. Wang, G. Yin, *Chem. Eng. J.* **2021**, *412*, 128617; d) J. Serrano-Sevillano, M. Casas-Cabanas, A. Saracibar, *J. Phys. Chem. Lett.* **2021**, *12*, 7474.

[25] M. Ohring, in *Materials Science of Thin Films (Second Edition)*, (Ed: M. Ohring), Academic Press, San Diego **2002**.

[26] P. Lours, F. Baillon, in *The heart of crystalline materials-Stacking faults and twins*, https://nte.mines-albi.fr/SciMat/en/co/SM3uc3-2.html (accessed: 2021).

[27] J. M. Thomas, P. A. Midgley, C. Ducati, R. K. Leary, *Prog. Nat. Sci.: Mater. Int.* **2013**, *23*, 222.

[28] G. Casillas, A. A. Gazder, E. V. Pereloma, A. A. Saleh, *Mater. Charact.* **2017**, *123*, 275.

[29] Y. B. Xue, Y. T. Zhou, D. Chen, X. L. Ma, *J. Alloys Compd.* **2014**, *582*, 181.

[30] M. Shih, J. Miao, M. Mills, M. Ghazisaeidi, *Nat. Commun.* **2021**, *12*, 3590.

[31] D. Hull, D. J. Bacon, *Introduction to Dislocation*, 5th ed., Elsevier, Butterworth-Heinemann **2011**.

[32] S. Kibey, J. B. Liu, D. D. Johnson, H. Sehitoglu, *Acta Mater.* **2007**, *55*, 6843.

[33] a) K. Edalati, Z. Horita, *Acta Mater.* **2011**, *59*, 6831; b) A. Rohatgi, K. S. Vecchio, G. T. Gray, *Metall. Mater. Trans. A* **2001**, *32*, 135; c) W. Woo, J. S. Jeong, D. K. Kim, C. M. Lee, S. H. Choi, J. Y. Suh, S. Y. Lee, S. Harjo, T. Kawasaki, *Sci. Rep.* **2020**, *10*, 1350; d) D. J. Siegel, *Appl. Phys. Lett.* **2005**, *87*, 121901; e) G. Xu, X. Chong, Y. Zhou, Y. Wei, C. Hu, A. Zhang, R. Zhou, J. Feng, *J. Mater. Res.* **2020**, *35*, 2718.

[34] Z. Gong, J. Liu, G. Ye, H. Fei, *Chem. Commun.* **2023**, *59*, 5661.

[35] M. Han, Z. Liu, X. Shen, L. Yang, X. Shen, Q. Zhang, X. Liu, J. Wang, H.-J. Lin, C.-T. Chen, C.-W. Pao, J.-L. Chen, Q. Kong, X. Yu, R. Yu, L. Gu, Z. Hu, X. Wang, Z. Wang, L. Chen, *Adv. Energy Mater.* **2020**, *10*, 2002631.

[36] F. Meng, M. Estruga, A. Forticaux, S. A. Morin, Q. Wu, Z. Hu, S. Jin, *ACS Nano* **2013**, *7*, 11369.

[37] C. Wang, Z. Zhang, G. Yang, Q. Chen, Y. Yin, M. Jin, *Nano Lett.* **2016**, *16*, 5669.

[38] M. Zhou, C. Cheng, C. Dong, L. Xiao, Y. Zhao, Z. Liu, X. Zhao, K. Sasaki, H. Cheng, X. Du, J. Yang, *Adv. Energy Mater.* **2023**, *13*, 2202595.

[39] J. Zhang, X. Li, X. Zhang, C. Cheng, L. Xiao, M. Zhou, C. Dong, H. Liu, X. Du, J. Yang, *Small Methods* **2023**, *7*, 2300461.

[40] Z. R. Ramadhan, A. R. Poerwoprajitno, S. Cheong, R. F. Webster, P. V. Kumar, S. Cychy, L. Gloag, T. M. Benedetti, C. E. Marjo, M. Muhler, D.-W. Wang, J. J. Gooding, W. Schuhmann, R. D. Tilley, *J. Am. Chem. Soc.* **2022**, *144*, 11094.

[41] R. Huang, Z. Sun, S. Chen, S. Wu, Z. Shen, X. Wu, J. Zeng, *Chem. Commun.* **2017**, *53*, 6922.

[42] L. Zhang, J. C. Yu, M. Mo, L. Wu, Q. Li, K. W. Kwong, *J. Am. Chem. Soc.* **2004**, *126*, 8116.

[43] a) R. Long, S. Zhou, B. J. Wiley, Y. Xiong, *Chem. Soc. Rev.* **2014**, *43*, 6288; b) C. Wang, X. Li, L. Jin, P.-H. Lu, C. Dejoie, W. Zhu, Z. Wang, W. Bi, R. E. Dunin-Borkowski, K. Chen, M. Jin, *Nano Lett.* **2019**, *19*, 6363; c) A. Mahmood, D. He, S. H. Talib, Y. He, Z. Song, L. Zhenbang, D. Han, L. Niu, *Adv. Funct. Mater.* **2022**, *32*, 2205223.

[44] a) Y. Sun, B. Gates, B. Mayers, Y. Xia, *Nano Lett.* **2002**, *2*, 165; b) Y. Sun, B. Mayers, T. Herricks, Y. Xia, *Nano Lett.* **2003**, *3*, 955.

[45] Y. Wang, H.-C. Peng, J. Liu, C. Z. Huang, Y. Xia, *Nano Lett.* **2015**, *15*, 1445.

[46] M. Xu, F. Yang, Y. Yuan, Q. Guo, B. Ren, J. Yao, R. Gu, *J. Colloid Interface Sci.* **2013**, *407*, 60.

[47] Y. Lu, J.-p. Tu, C.-d. Gu, X.-h. Xia, X.-l. Wang, S. X. Mao, *J. Mater. Chem.* **2011**, *21*, 4843.

[48] C. Salzemann, J. Urban, I. Lisiecki, M.-P. Pileni, *Adv. Funct. Mater.* **2005**, *15*, 1277.

[49] V. V. Radmilović, J. Kacher, E. R. Ivanović, A. M. Minor, V. R. Radmilović, *Cryst. Growth Des.* **2016**, *16*, 467.

[50] C. Tang, P. Gong, T. Xiao, Z. Sun, *Nat. Commun.* **2021**, *12*, 2139.

[51] L. Fang, S. Wang, C. Song, S. Lu, X. Yang, X. Qi, H. Liu, *Chem. Eng. J.* **2022**, *446*, 137341.

[52] X. Zhang, X. Li, Z. Pan, Y. Lai, Y. Lu, Y. Wang, S. Song, *Chem. Eng. J.* **2021**, *426*, 131524.

[53] A. G. Butterfield, L. T. Alameda, R. E. Schaak, *J. Am. Chem. Soc.* **2021**, *143*, 1779.

[54] M. A. Domínguez-Crespo, M. Plata-Torres, A. M. Torres-Huerta, E. M. Arce-Estrada, J. M. Hallen-López, *Mater. Charact.* **2005**, *55*, 83.

[55] R. Su, Z. Wang, L. Zhu, Y. Pan, D. Zhang, H. Wen, Z.-D. Luo, L. Li, F.-t. Li, M. Wu, L. He, P. Sharma, J. Seidel, *Angew. Chem., Int. Ed.* **2021**, *60*, 16019.

[56] B. Liu, J. Wang, D. Mou, J. Fu, W. Chen, Z. Fu, Q. Qiang, L. Peng, L. Zhao, J. Wei, J. Qiu, C. Ma, *J. Alloys Compd.* **2021**, *850*, 156737.

[57] J. Zhang, X. Li, X. Zhang, C. Cheng, L. Xiao, M. Zhou, C. Dong, H. Liu, X. Du, J. Yang, *Small Methods* **2023**, *7*, 2300461.

[58] W. Peng, Z. Wang, R. Lu, Q. Li, Z. Wang, Y. Zhao, L. Xu, L. Mai, *Chem. Eng. J.* **2023**, *457*, 141173.

[59] K. He, M. Wang, L. Guo, *Chem. Eng. J.* **2015**, *279*, 747.

[60] Y. Li, L. Tang, S. Peng, Z. Li, G. Lu, *CrystEngComm* **2012**, *14*, 6974.

[61] K. He, L. Guo, *Int. J. Hydrogen Energy* **2017**, *42*, 23995.

[62] M. Liu, D. Jing, Z. Zhou, L. Guo, *Nat. Commun.* **2013**, *4*, 2278.

[63] M. Chen, P. Wu, Y. Zhu, S. Yang, Y. Lu, Z. Lin, *Int. J. Hydrogen Energy* **2018**, *43*, 10938.

[64] B. Gong, Y. Lu, P. Wu, Z. Huang, Y. Zhu, Z. Dang, N. Zhu, G. Lu, J. Huang, *Appl. Surf. Sci.* **2016**, *365*, 280.

[65] J. Chen, W. Tang, L. Xin, Q. Shi, *Appl. Phys. A* **2011**, *102*, 213.

[66] J.-Y. Hao, Y.-Y. Wang, X.-L. Tong, G.-Q. Jin, X.-Y. Guo, *Catal. Today* **2013**, *212*, 220.

[67] A. Ozawa, M. Yamamoto, T. Tanabe, S. Hosokawa, T. Yoshida, *J. Mater. Chem. A* **2020**, *8*, 7368.

[68] a) Y. Wang, B. Liu, X. Shen, H. Arandiyan, T. Zhao, Y. Li, M. Garbrecht, Z. Su, L. Han, A. Tricoli, C. Zhao, *Adv. Energy Mater.* **2021**, *11*, 2003759; b) Y. Wang, X. Shen, H. Arandiyan, Y. Yin, F. Sun, X. Chen, M. Garbrecht, L. Han, G. G. Andersson, C. Zhao, *J. Power Sources* **2020**, *478*, 228748; c) H. Arandiyan, S. S. Mofarah, Y. Wang, C. Cazorla, D. Jampaiah, M. Garbrecht, K. Wilson, A. F. Lee, C. Zhao, T. Maschmeyer, *Chem. Eur. J.* **2021**, *27*, 14418; d) T. Zhao, Y. Wang, X. Chen, Y. Li, Z. Su, C. Zhao, *ACS Sustainable Chem. Eng.* **2020**, *8*, 4863; e) C. Qiu, F. Cai, Y. Wang, Y. Liu, Q. Wang, C. Zhao, *J. Colloid Interface Sci.* **2019**, *565*, 351.

[69] a) C. Rong, K. Dastafkan, Y. Wang, C. Zhao, *Adv. Mater.* **2023**, *35*, 2211884; b) T. Zhao, X. Shen, Y. Wang, R. K. Hocking, Y. Li, C. Rong, K. Dastafkan, Z. Su, C. Zhao, *Adv. Funct. Mater.* **2021**, *31*, 2100614; c) Z. Gong, R. Liu, H. Gong, G. Ye, J. Liu, J. Dong, J. Liao, M. Yan, J. Liu, K. Huang, L. Xing, J. Liang, Y. He, H. Fei, *ACS Catal.* **2021**, *11*, 12284.

[70] J. Kang, G. Liu, Q. Hu, Y. Huang, L.-M. Liu, L. Dong, G. Teobaldi, L. Guo, *J. Am. Chem. Soc.* **2023**, *145*, 25143.

[71] H. Pang, Z. Yu, X. Qin, B. Fan, R. Jiang, S. Li, Y. Hou, W. Tang, M. Wang, Z. Shi, *J. Colloid Interface Sci.* **2023**, *646*, 503.

[72] J. Bak, H. B. Bae, J. Kim, J. Oh, S.-Y. Chung, *Nano Lett.* **2017**, *17*, 3126.

[73] Q. Mou, Z. Xu, W. Zuo, T. Shi, E. Li, G. Cheng, X. Liu, H. Zheng, H. Li, P. Zhao, *Mater. Chem. Front.* **2022**, *6*, 2750.

[74] A. K. Tomar, U. N. Pan, N. H. Kim, J. H. Lee, *ACS Energy Lett.* **2023**, *8*, 565.
[75] S. Zhao, M. Li, M. Han, D. Xu, J. Yang, Y. Lin, N.-E. Shi, Y. Lu, R. Yang, B. Liu, Z. Dai, J. Bao, *Adv. Funct. Mater.* **2018**, *28*, 1706018.
[76] J. Tang, J. L. Xu, Z. G. Ye, X. B. Li, J. M. Luo, *J. Mater. Sci. Technol.* **2021**, *79*, 171.
[77] K. Huang, D. Peng, Z. Yao, J. Xia, B. Zhang, H. Liu, Z. Chen, F. Wu, J. Wu, Y. Huang, *Chem. Eng. J.* **2021**, *425*, 131533.
[78] K. Huang, B. Zhang, J. Wu, T. Zhang, D. Peng, X. Cao, Z. Zhang, Z. Li, Y. Huang, *J. Mater. Chem. A* **2020**, *8*, 11938.
[79] G. Zhang, J. Yuan, Y. Liu, W. Lu, N. Fu, W. Li, H. Huang, *J. Mater. Chem. A* **2018**, *6*, 10253.
[80] L. Gloag, T. M. Benedetti, S. Cheong, Y. Li, X.-H. Chan, L.-M. Lacroix, S. L. Y. Chang, R. Arenal, I. Florea, H. Barron, A. S. Barnard, A. M. Henning, C. Zhao, W. Schuhmann, J. J. Gooding, R. D. Tilley, *Angew. Chem., Int. Ed.* **2018**, *57*, 10241.
[81] a) J. D. Butson, A. Sharma, J. Tournet, Y. Wang, R. Tatavarti, C. Zhao, C. Jagadish, H. H. Tan, S. Karuturi, *Adv. Energy Mater.* **2023**, *13*, 2301793; b) J. D. Butson, A. Sharma, H. Chen, Y. Wang, Y. Lee, P. Varadhan, M. N. Tsampas, C. Zhao, A. Tricoli, H. H. Tan, C. Jagadish, S. Karuturi, *Adv. Energy Mater.* **2022**, *12*, 2102752; c) C. Qiu, S. He, Y. Wang, Q. Wang, C. Zhao, *Chemistry* **2020**, *26*, 4120.
[82] a) Y. Wang, H. Arandiyan, X. Chen, T. Zhao, X. Bo, Z. Su, C. Zhao, *J. Phys. Chem. C* **2020**, *124*, 9971; b) T. Zhao, Y. Wang, S. Karuturi, K. Catchpole, Q. Zhang, C. Zhao, *Carbon Energy* **2020**, *2*, 582; c) Y. Wang, H. Arandiyan, K. Dastafkan, Y. Li, C. Zhao, *Chem. Res. Chin. Univ.* **2020**, *36*, 360.
[83] B. Hammer, J. K. Nørskov, in *Advances in Catalysis*, Vol. *45*, Academic Press, San Diego, **2000**.
[84] Y. Pi, Y. Xu, L. Li, T. Sun, B. Huang, L. Bu, Y. Ma, Z. Hu, C.-W. Pao, X. Huang, *Adv. Funct. Mater.* **2020**, *30*, 2004375.
[85] X. Zhang, Y. Yang, Y. Liu, Z. Jia, Q. Wang, L. Sun, L. C. Zhang, J. J. Kruzic, J. Lu, B. Shen, *Adv. Mater.* **2023**, *35*, 2303439.
[86] E. T. Nguyen, I. A. Bertini, A. J. Ritz, R. A. Lazenby, K. Mao, J. R. McBride, A. V. Mattia, J. E. Kuszynski, S. F. Wenzel, S. D. Bennett, G. F. Strouse, *Inorg. Chem.* **2022**, *61*, 13836.
[87] Y. Ye, H. Li, J. Cao, X. Liu, H. Fan, M. Wei, L. Yang, J. Yang, Y. Chen, *Int. J. Hydrogen Energy* **2023**, *48*, 17026.
[88] J. Wang, J. Huang, G. Chen, W. Chen, T. Li, A. Meng, K. Ostrikov, *Chem. Eng. J.* **2022**, *446*, 137297.
[89] C. S. Jung, K. Park, Y. Lee, I. H. Kwak, I. S. Kwon, J. Kim, J. Seo, J.-P. Ahn, J. Park, *CrystEngComm* **2019**, *21*, 1143.
[90] X. Cui, Z. Zhang, Y. Gong, F. Saleem, B. Chen, Y. Du, Z. Lai, N. Yang, B. Li, L. Gu, H. Zhang, *CCS Chem.* **2020**, *2*, 24.
[91] R. Chattot, T. Asset, P. Bordet, J. Drnec, L. Dubau, F. Maillard, *ACS Catal.* **2017**, *7*, 398.
[92] a) X. Feng, K. Jiang, S. Fan, M. W. Kanan, *J. Am. Chem. Soc.* **2015**, *137*, 4606; b) F. Hu, S. C. Abeyweera, J. Yu, D. Zhang, Y. Wang, Q. Yan, Y. Sun, *Chem* **2020**, *6*, 3007.
[93] D. Kudo, S. Kaneko, R. Myochi, Y. Chida, N. Todoroki, T. Tanabe, T. Wadayama, *ACS Appl. Energy Mater.* **2019**, *2*, 4597.
[94] J. Serrano-Sevillano, V. Charbonnier, N. Madern, M. Latroche, C. Magén, V. Serin, J. Monnier, M. Casas-Cabanas, J. Zhang, *Chem. Mater.* **2022**, *34*, 4568.
[95] J.-Y. Lin, C. Xi, Z. Li, Y. Feng, D.-Y. Wu, C.-K. Dong, P. Yao, H. Liu, X.-W. Du, *Chem. Commun.* **2019**, *55*, 3121.

Yuan Wang (Helena) is a Senior Lecturer and ARC-DECRA Fellow at the Department of Chemical Engineering at the University of Melbourne. She completed her Ph.D. in Chemical Engineering at the University of New South Wales (UNSW) in 2018. She held prestigious fellowships: the Alfred Deakin Research Fellowship-2022 at Deakin University and the International Hydrogen Research Fellowship-2023 at the National University of Singapore. She was also a DAAD Visiting Scholar at the Fritz Haber Institute of Max Planck-Berlin (2018). Her research focuses on green hydrogen production, carbon dioxide conversion and utilization, metal recovery and recycling, and circular economy.

Tian Wang received her B. Eng. and M. Eng. degrees in Chongqing University. She is currently a Ph.D. candidate at the Department of Chemical and Biomolecular Engineering, National University of Singapore. Her research interest focuses on electrocatalysts for CO_2 reduction reactions.

Hamidreza Arandiyan is a leader of Critical Minerals for Clean Energy Group and has an academic tenure in Applied Chemistry and Environmental Science at RMIT University. He completed his Ph.D. from the School of Environment at Tsinghua University in 2014. He received a Vice-Chancellor's Research Fellowship from the University of New South Wales at the School of Chemical Engineering in 2015. He held a University of Sydney Senior VC Fellowship in the School of Chemistry in 2018. He is a Fellow of the Royal Society of Chemistry (FRSC). His research focuses on resource recovery for environmental remediation and energy applications.

Guoqiang Song received his Ph.D. from the School of Chemistry and Chemical Engineering at the Taiyuan Institute of Technology in 2016. He became an Associate Professor at Guizhou Institute of Technology in 2018. He then worked as a research fellow at the Department of Chemical & Biomolecular Engineering, National University of Singapore from 2022. His research predominantly focuses on the concurrent development of catalysts for CO_2 and CH_4 utilization, along with membranes designed for the selective separation of H_2 and H_2O from various gases.

Hongyu Sun received his Ph.D. degree from the State Key Laboratory of Metastable Materials Science and Technology, Yanshan University, in 2010. He then worked in the Department of Materials Science and Engineering (2010-2012), Beijing National Centre for Electron Microscopy (2012-2015), at Tsinghua University (with Prof. Jing Zhu), Department of Micro- and Nanotechnology at the Technical University of Denmark (2015-2018, with Prof. Kristian Mølhave). Now, he is a senior application scientist at DENSsolution B.V. His research interests include controllable synthesis of functional structures for energy storage and conversion, liquid cell transmission electron microscopy, and microfabrication.

Ylias Sabri is a chemical engineer (B. Eng, Hons.) by training and completed Ph.D. in 2010. Currently, he is a senior lecturer at RMIT University's Chemical and Environmental Engineering department. He holds a visiting Scientist fellowship at Commonwealth Scientific and Industrial Research Organization (CSIRO), is a member of Mercury Australia, and is on the Editorial board of Micromachines and Journal of Sensors. He co-manages the Nanotechnology and Chemical Sensor group at RMIT University, where his research focuses on chemical sensors, pollution control technology, and catalyst development. One of his inventions includes a hydrogen gas sensor (WO2022087683), which is undergoing a commercialization process.

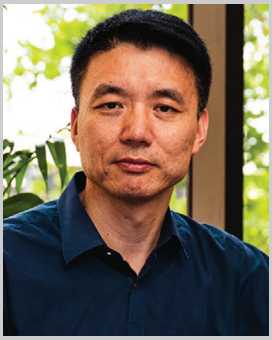

Chuan Zhao is a Professor at the School of Chemistry at the University of New South Wales (UNSW), Sydney. He also holds a Professorial Future Fellowship from the Australian Research Council. He is interested in discovering novel electrochemical methodologies and nanomaterials for energy applications, including water splitting, hydrogen fuel cells, CO_2 & N_2 reduction, batteries, and sensors.

Zongping Shao is a Professor of Chemical Engineering at Curtin University, Australia, and Nanjing Tech University, China. He obtained his Ph.D. from the Dalian Institute of Chemical Physics, China, in 2000. He worked as a Visiting Scholar at the Institut de Researches sur la Catalyse, CNRS, France, and as a Postdoctoral Research Fellow at the California Institute of Technology, USA, from 2000 to 2005. His research interests include solid oxide fuel cells, lithium-ion batteries, supercapacitors, and low-temperature energy-conversion devices. Elsevier has recognized him as a Highly Cited Researcher in the Energy section since 2015.

Sibudjing Kawi obtained his Bachelor's, Master's, and Ph.D. degrees, as well as completed his Post-doc at the University of Texas at Austin, the University of Illinois at Urbana-Champaign, the University of Delaware, and the University of California at Davis, respectively, prior to joining the National University of Singapore. His research primarily revolves around integrating catalysts with membranes to address energy and environmental issues, focusing on addressing challenges related to CO_2 and H_2 through the utilization of biomass waste and natural gas. He is recognized as the World's Most Highly Cited Researcher for the years 2021 and 2022, according to Clarivate.